Leopold-Franzens University of Innsbruck

Laser system for the Rydberg excitation of Strontium ions

A Thesis
submitted to the Faculty of
Mathematics, Computer Science and Physics,
in partial fulfillment of the requirements
for the degree of

MASTER OF SCIENCE

carried out at the Institute of Experimental Physics
under the guidance of assoz. Prof. Dr. Markus Thomas Hennrich,
presented by

CHRISTINE MAIER

November 2013

Alle sagten: „Das geht nicht.“
Dann kam einer, der wusste das nicht und hat’s gemacht.

Unbekannt

Kurzfassung

Gefangene Rydberg Ionen stellen einen neuen, vielversprechenden Ansatz in der Quanteninformationsverarbeitung dar, wurden jedoch bisher noch nicht experimentell erforscht. Die vorliegende Masterarbeit befasst sich mit den experimentellen Grundlagen zur Anregung von Strontiumionen in den Rydbergzustand. Das Hauptaugenmerk liegt auf der Realisierung des Lasersystems zur Rydberganregung, anhand eines zwei-Photonen-Übergangs, und der Charakterisierung des erzeugten Laserlichts.

Einer der benötigten UV-Anregungslaser ist nicht handelsüblich erhältlich und wird daher über Summenfrequenzmischung (SFG) und anschließender Frequenzverdopplung (SHG) erzeugt. Im SFG-Prozess werden ein 1551 nm und ein verstimmbarer 1000 nm Diodenlasers in einem Lithiumniobat-Kristall gemischt um Laserlicht mit 607-619 nm zu erzeugen, welches schließlich im SHG-Prozess zu 304-310 nm frequenzverdoppelt wird. Dank der verstimmbaren Wellenlänge dieses Anregungslasers wird es möglich sein die Strontiumionen in Rydbergzustände mit einer Hauptquantenzahl über $n = 30$ (bis hin zu zweifacher Ionisation) anzuregen.

Abstract

Trapped Rydberg ions represent a new, promising approach to quantum information processing but have yet to be experimentally realized. The present master thesis treats the experimental basis for the excitation of strontium ions into the Rydberg state. The main focus is the realization of the laser system for the two-photon Rydberg excitation and the characterization of the generated laser light.

One of the two UV excitation lasers is not commercially available and is therefore generated by successive sum-frequency generation (SFG) and second-harmonic generation (SHG). In the SFG process a 1551 nm diode laser and a tunable 1000 nm diode laser are mixed in a lithium niobate crystal to generate 607-619 nm laser light, which is then frequency-doubled to 304-310 nm in a SHG system. Based on the tunability of this excitation laser, it will be feasible to excite trapped strontium ions into Rydberg states with principal quantum numbers above $n = 30$ (up to double ionization).

Contents

Chapter 1

Introduction

Quantum information processing represents a successful and rapidly growing field in physics. The aim is to develop quantum computers for simulating complicated quantum systems (e.g. many-body systems), performing extensive calculations fast (e.g. factorization), and efficiently searching large databases. In contrary to classical computers, which use macroscopic currents switched by transistors, the bits of a quantum computer are formed by two-level quantum-mechanical objects, so called "qubits". Such two-level systems are for example represented by the polarization of a photon, the spin state of an electron, or the electronic state of an atom/ion. The advantage of a qubit is that it is not restricted to be in one state or the other ('0' or '1') but it can be in a superposition of both basis states simultaneously ($|\Psi\rangle = \alpha\,|0\rangle + \beta\,|1\rangle$). This means that a system of n qubits can be in a superposition of 2^n different states, so it can store exponentially more information than a classical system and perform 2^n calculations simultaneously. In 1996, D. P. Di Vincenzo published the following five requirements of a quantum computer [1]:

1. A scalable physical system with well-defined qubits
2. Ability to initialize the qubit states efficiently
3. Long decoherence times, much longer than gate-operation times, and/or protocols which are insensitive to decoherence caused by environment interaction (quantum error correction)
4. Universal set of quantum operations, for example consisting of: single-qubit rotations and two qubit gates (entanglement)
5. Possibility to read out the qubit state by a strong measurement

Cooled, trapped ions are one of the most advanced systems currently being investigated for quantum information processing. Their qubit basis states are represented by ground and metastable states and they exhibit relatively long coherence times and an exceptional ability of quantum control [2–5]. This makes them a useful system for quantum information processing. Nevertheless, the scalability criterion and the gate operation time still need to be improved[1]: One of the largest quantum registers was produced in the research team of Rainer Blatt in Innsbruck [6], where they realized entanglement of 14 calcium ions in a linear Paul trap. In these experiments

[1] Typical parameters [6] for trapped ions are a duration time of an entangling gate of around $50\,\mu s$ and a single qubit coherence time of 100 ms.

entanglement operations use the common motional modes of an ion string as a phonon data bus for information transfer. For this the motional sidebands have to be spectroscopically resolved, which limits the gate operation time since the spectral width of the exciting laser pulse has to be smaller than the distance between the motional modes. Moreover, the motional mode spectrum becomes significantly larger with increasing number of involved particles and it gets more and more difficult to address the individual modes.

An alternative, promising approach is the extension of low-level trapped ions to highly excited trapped ions - so called "Rydberg" ions. The outer valence electron of a Rydberg ion is excited to states with large principal quantum number n such that the particle transforms into a macroscopic-sized object with several hundred nanometres in diameter, $d_{Ryd} \sim n^2$ [7].

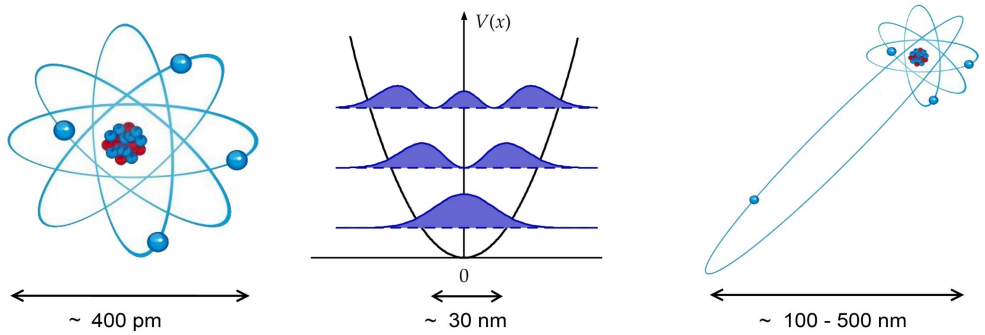

Figure 1.1: Size comparison. From left to right: ion, typical harmonic motional wave functions in a linear Paul trap, Rydberg ion. The size of a Rydberg ion is around one order of magnitude larger than the typical extension of the motional ground state wave function in a linear Paul trap and around three orders of magnitude larger than the ground state ion itself.

The large orbital radius of the valence electron leads to a strong polarizability $\alpha \sim n^7$ of Rydberg ions. Therewith one expects strong Van der Waals interaction $\sim n^{11}/r^6$ at large distances and strong dipole-dipole interaction $\sim n^4/r^3$ at smaller distances. In 2008, a group of researchers led by P. Zoller [8] explored the idea of fast Rydberg gates in an ion chain in detail. They pointed out that Rydberg ions, which are aligned in a Wigner crystal, do not exhibit permanent dipole moments. For typical trapping parameters [9] also the Van der Waals interaction between the Rydberg ions is small compared to the linewidth of the Rydberg states and the external trapping frequencies of the ions. Thus, P. Zoller and co-workers proposed to increase the interaction strength of Rydberg ions by applying off-resonant microwave fields, coupling the electronic Rydberg states $|n', p\rangle$ and $|n, s\rangle$ (Fig. 1.2). This coupling results in an effective dressed state

$$|s'\rangle = |n, s\rangle - \frac{\Omega_{\mathrm{MW}}}{2\Delta} |n', p\rangle \quad ,$$

where the weak admixture of $|n', p\rangle$ leads to a large, oscillating dipole moment on the $|s'\rangle$ state: $d \sim \frac{\Omega_{\mathrm{MW}}}{\Delta} e a_0 n^2 cos(wt) \approx 3000$ D (c.f. dipole moment from trapped ion motion: $d \approx 350$ D). This induces a strong dipole-dipole interaction between Rydberg ions. The microwave transition frequency lies typically in the order of tens to hundreds of gigahertz and does not couple to the external motion of the ions (lying in the megahertz regime).

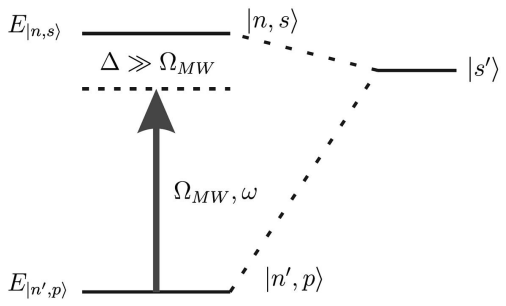

Figure 1.2: Scheme of the microwave dressing of ionic Rydberg states. An off-resonant microwave field couples $|n,s\rangle$ and $|n',p\rangle$ Rydberg levels and generates an effective dressed state $|s'\rangle$ with oscillating dipole moment.

A very important consequence of the strong interactions in Rydberg systems is the Rydberg-blockade. This dipole-blockade acts within a certain "blockade radius", preventing the excitation of more than one atom into the Rydberg state: A Rydberg atom shifts the Rydberg energy levels of neighboring atoms such that they are out of resonance with respect to the narrow[2] and primarily resonant excitation laser (Fig. 1.3). Therefore, the excitation of a second nearby atom into the Rydberg state is blocked.

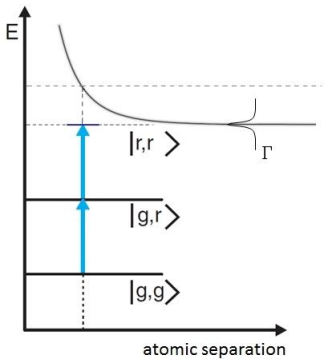

Figure 1.3: Energy level scheme illustrating the Rydberg blockade on a two-atom system. $|g,g\rangle$: state with both atoms in a low-lying state, $|g,r\rangle$: one atom is excited to a Rydberg state, $|r,r\rangle$: common state of two neighboring Rydberg atoms. The state $|r,r\rangle$ is shifted out of resonance to the excitation laser due to the interaction between the Rydberg atoms. The atomic linewidth of the $|r,r\rangle$ state results from the spontaneous decay Γ and is smaller than the interaction-induced energy shift.

In 2000, Jaksch et al. [10] proposed fast quantum gates for neutral atoms, based on the Rydberg blockade. Employing this principle with trapped Rydberg ions allows for quantum gates independent from the external motional dynamics of the ions. The basic idea for a Rydberg-blockade mediated two-qubit phase gate is depicted in Fig. 1.4:

[2]The linewidth of the Rydberg excitation laser has to be smaller than the interaction-induced and inter-atomic distance dependent energy shift.

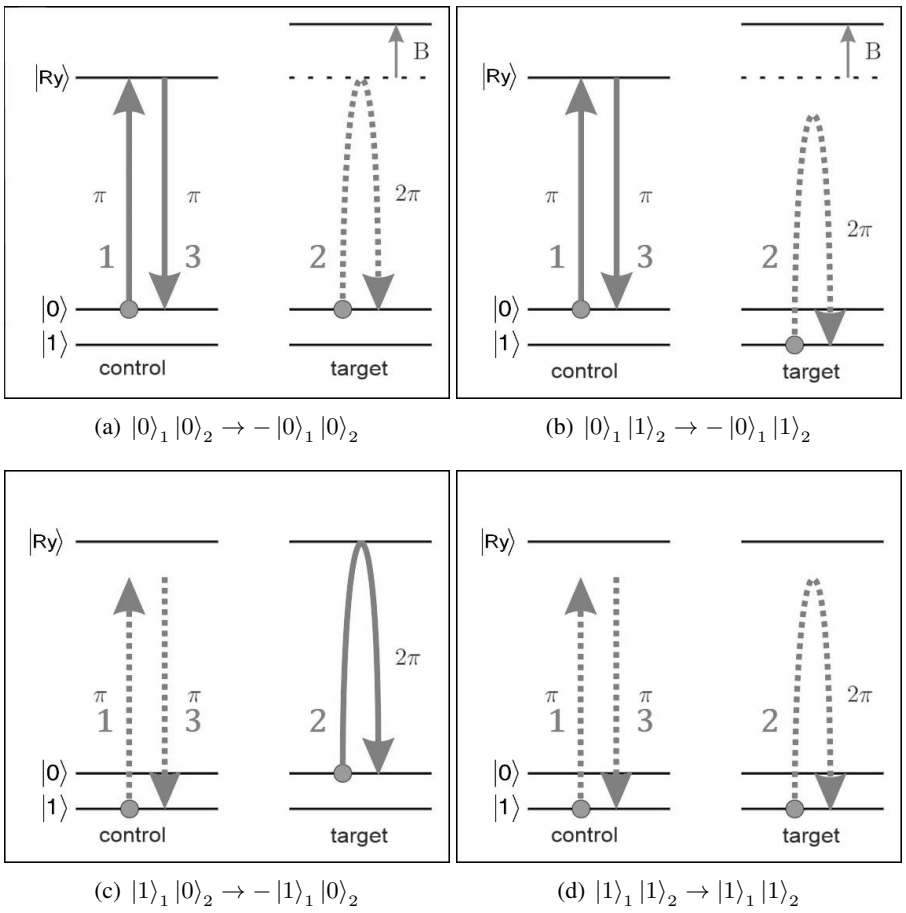

(a) $|0\rangle_1 |0\rangle_2 \rightarrow -|0\rangle_1 |0\rangle_2$

(b) $|0\rangle_1 |1\rangle_2 \rightarrow -|0\rangle_1 |1\rangle_2$

(c) $|1\rangle_1 |0\rangle_2 \rightarrow -|1\rangle_1 |0\rangle_2$

(d) $|1\rangle_1 |1\rangle_2 \rightarrow |1\rangle_1 |1\rangle_2$

Figure 1.4: Rydberg-blockade mediated conditional phase gate on two atoms, realized by the pulse sequence $\pi_{\text{control}} \rightarrow 2\pi_{\text{target}} \rightarrow \pi_{\text{control}}$. As explained in the text below, the Rydberg excitation of the control atom induces an energy shift B of the Rydberg level $|Ry\rangle$ for the target atom such that its excitation is blocked.

Consider a two-atom system and a narrow laser, resonant only to a single-atom transition from an upper ground state $|0\rangle$ to a Rydberg state $|Ry\rangle$. If the two-atom system is initially in the $|0\rangle |0\rangle$ state (case a) or $|0\rangle |1\rangle$ state (case b) a π pulse on the control atom shifts the energy of the double Rydberg state, such that the excitation laser is far off-resonant (in case (b) it is anyway off-resonant) and is not able to excite the target atom into the Rydberg state $|Ry\rangle$. Thus, a 2π pulse on the target atom leaves the system practically unaffected. A subsequent π pulse on the first atom returns the system back to the initial state, except of a sign change in the wave function. If the system is arranged in the $|1\rangle |0\rangle$ state (case c), the laser cannot drive a transition from the lower ground state $|1\rangle$ to the Rydberg state on the control atom since it is not resonant. Therefore the Rydberg excitation of the target atom is not blocked and an applied 2π pulse causes a π phase shift (sign change) to the wave function. Only case d, with both atoms being in the lower ground state $|1\rangle |1\rangle$ does not accumulate any phase because the off-resonant laser can not drive any excitation. Summed up, the entire pulse-sequence corresponds to a controlled phase gate (C_Z). The Rydberg energy shift lies in the megahertz-regime and the decay rate of

a Rydberg state measures a few microseconds. Therefore, we can apply relatively high Rabi frequencies and thus perform gate operations within nanoseconds or a few microseconds.

The ability to perform any unitary operation on a quantum computer requires a complete set of universal gates. Such a set can be represented by a combination of single qubit rotations and two-qubit controlled-NOT (CNOT) gates [11]. The first realizations of CNOT gates, based on the Rydberg blockade, were demonstrated in [12] with neutral atoms. One standard approach is to apply Hadamard rotations on the target atom before and after a controlled phase gate. The entire pulse-sequence takes 7 µs and results in the so called H-C_Z CNOT gate (Fig. 1.5).

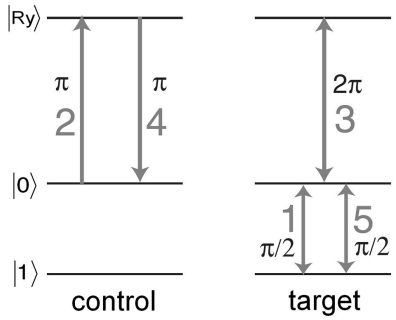

Figure 1.5: Schematic H-C_Z CNOT gate, realized with neutral atoms [12].

Using the Rydberg interaction for two-ion gates has several advantages: As we have seen above, the strong long-range interactions allow dynamical processes (such as quantum gates) to run on the nanosecond or low-microsecond time scale, which is much faster than the time scale for external motional processes. Another advantage over other dipolar systems is that the Rydberg interaction strengths can be controlled, and even turned on and off, by exciting the electron to the corresponding Rydberg level or not. All these are convincing arguments to choose this approach as an extension of cooled, trapped ions towards the long-term goal of a *quantum computer*. Our group aims to trap and cool strontium ions and excite them into a Rydberg state in order to experimentally investigate the behaviour and interaction properties of Rydberg ions and analyze their suitability as a system for quantum simulation and quantum information processing.

This thesis describes the laser system for the excitation of strontium ions into Rydberg states. It is structured as follows: Chapter 2 summarizes a theoretical characterization of the wave functions and lifetimes of the most relevant strontium energy levels as well as an estimation of the required Rabi frequencies and laser linewidths. It also treats some nonlinear optical phenomena, which are fundamental for our Rydberg excitation scheme. Chapter 3 introduces three technical principles for the experimental realization of the theoretical ideas: periodically poled crystals and the Sellmeier equation, the optimized focusing into the nonlinear crystal, and the ring resonator. Chapter 4 focuses on the experimental setup for the generation and stabilization of the required Rydberg excitation laser light and discusses technical characteristics and simulations. Finally, chapter 5 summarizes the main results and gives an outlook on future applications. The appendices present two Mathematica programs, containing basic calculations for the laser system setup.

Chapter 2

Theoretical background

2.1 Strontium energy levels

Strontium is an alkaline earth metal with electronic configuration [Kr]$5s^2$, thus it has two valence electrons. After single ionization, it has similar properties to the hydrogen atom, so it is easy to theoretically describe its behaviour and manipulate its states.

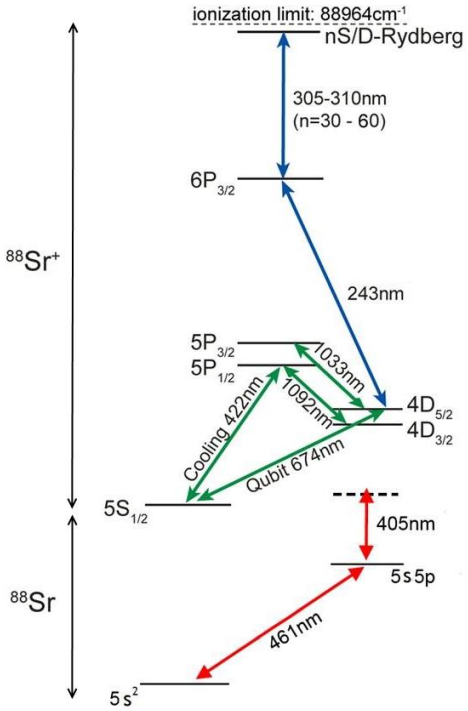

Figure 2.1: Relevant energy levels of strontium and the corresponding laser system. The lowest two levels shown belong to the neutral strontium atom. The ionization lasers (red arrows) excite one valence electron to a metastable state above the ionization limit from which it is spontaneously emitted, leaving a strontium ion behind (autoionization). The green arrows denote the lasers for trapping, cooling and state manipulation. Blue arrows represent the two UV lasers for the planned excitation into a nS/D Rydberg state with quantum number n between 30 and 60.

Fig. 2.1 shows the strontium energy levels which are relevant for our experiment. The 422 nm laser drives an almost closed dipole transition with rapid excitation and spontaneous decay. Therefore, the 422 nm photon scattering rate is very high, making this transition suitable for state detection and Doppler cooling. The ionic qubit is stored in the $5S_{1/2} \equiv |0\rangle$ ground state and the $4D_{5/2} \equiv |1\rangle$ metastable state, which can be manipulated via 674 nm light. In order to bring population quickly from $|1\rangle$ back to $|0\rangle$, i.e. state initiation, 1033 nm laser light artificially shortens the lifetime of the $4D_{5/2}$ state by exciting population to the short-lived $5P_{3/2}$ state from which it decays spontaneously to $5S_{1/2}$. Based on this, the 674 nm qubit laser and the 1033 nm laser will also be used to perform sideband cooling. The 1092 nm laser light serves as repumper in the cooling and state initialization processes.

The two blue arrows denote the UV lasers for the two excitation steps into the Rydberg state, with $6P_{3/2}$ as an intermediate level. A detuning in the GHz-regime[1] prevents populating the $6P_{3/2}$ state, from which spontaneous decay would reduce the Rydberg excitation efficiency. The tunable wavelength between 305-310 nm allows for excitation to nS and nD states with principal quantum numbers between $n = 30 - 60$ in order to experimentally explore and study this entire highly-excited region. The generation of the Rydberg excitation light is based on principles of nonlinear optics (Sec. 2.2) and is described in detail in chapter 4. At the submission of this thesis, the ion trap is under construction, as a result the laser system is yet to be directly tested.

The reason for choosing a two-photon instead of a single-photon excitation is the large energy gap between the upper qubit level and Rydberg levels. This corresponds to a laser wavelength of 135 nm which is absorbed in air. Besides the difficulties in generating such short wavelength lasers, handling such lasers is also technically demanding, since the setup has to be held in vacuum [14]. One advantage of strontium is the intermediate $6P_{3/2}$ level, which allows the excitation to be split into two steps. Moreover, wavelengths similar to the ones we require have been successfully produced in other experiments [15, 16]. Although Rydberg series in strontium ions were already investigated [17], we are working on the experimental setup towards the first realization of *trapped* Rydberg ions.

2.1.1 Wave functions and lifetimes

The following contains a short draft of the basic formulas and mathematical relations [14] for the theoretical characterization of the Sr^+ energy levels. In 2011, Weibin Li[2] used this theory to derive energies, wave functions, and lifetimes for the strontium ion. The idea is to reduce the many-body problem of the valence electron, inner electrons, and nucleus to a two-body problem, where the nucleus and the inner electrons are approximated as one doubly ionized core with a spherically symmetric potential. The valence electron is confined in this potential and the external ion-trapping potential. The dynamics of the trapped electron-ion system can be approximated by the two-body Hamiltonian, treated in the center-of-mass-frame

[1] The population of the intermediate level is negligible [13] if the detuning $|\Delta| \gg \sqrt{|\Omega_1(t)|^2 + |\Omega_2(t)|^2}$ and $|\Delta| \gg \Gamma_{\text{interm}}$, with the Rydberg transition Rabi frequencies $\Omega_{1,2}$ (given by Eq. 2.3) and the linewidth of the intermediate level Γ_{interm}.

[2] At this time postdoctoral researcher in the Theoretical Quantum physics department at the School of Physics and Astronomy, University of Nottingham.

$$
\begin{aligned}
H = & \frac{\mathbf{P_I^2}}{2M} + e\Phi(\mathbf{R},t) \\
& + \frac{\mathbf{p_e^2}}{2m_e} + V(|\mathbf{r}|) + V_{l,s}(\mathbf{r}) - e\Phi(\mathbf{r},t) \\
& - 2e\left[\alpha cos(\Omega t)(Xx - Yy) - \beta(Xx + Yy - 2Zz)\right]
\end{aligned}
$$

The first line represents the Hamiltonian for the center of mass (CM) motion in the trapping potential $\Phi(\mathbf{R},t)$, the second line describes the dynamics of the electron in the field of the doubly charged ion core and the superimposed trapping potential. The third line gives the electron-ion coupling due to their common motion in the trap. This results in an additional potential for the ion, which can be neglected for low-lying states $n < 10$. The interaction $V(|\mathbf{r}|)$ of the valence electron with the inner shell electrons and the nucleus can be approximated by an angular-momentum-dependent model potential [18]

$$
V_l(r) = -\frac{1}{r}\left[2 + (Z-2)e^{-\alpha_{l,1}r} + \alpha_{l,2} r e^{-\alpha_{l,3}r}\right] - \frac{\alpha_{c,p}}{2r^4}\left[1 - e^{-(r/r_l)^6}\right] \quad ,
$$

with the nuclear charge Z and the experimental dipole polarizability of the doubly charged ion $\alpha_{c,p} = 7.5$. Tab. 2.1 lists the parameters $\alpha_{l,i}$ and r_l, which were empirically determined by fitting the theoretical formulas, derived from the model potential, to known energy levels:

l	$\alpha_{l,1}$	$\alpha_{l,2}$	$\alpha_{l,3}$	r_l
0	3.4187	4.7332	1.5915	1.7965
1	3.3235	2.2539	1.5712	1.3960
2	3.2533	3.2330	1.5996	1.6820
$\geq$3	5.3540	7.9517	5.6624	1.0057

Table 2.1: Empirically determined parameters for the perturbing potential of a doubly ionized strontium core [18].

The Hamiltonian for the spin-orbit interaction is then described by

$$
V_{l,s}^{(so)}(r) = \frac{\alpha_{ls}^2 \boldsymbol{l}\cdot\boldsymbol{s}}{2r}\frac{dV_l(r)}{dr}\left[1 - \frac{\alpha_{ls}^2}{2}V_l(r)\right]^{-2} \quad ,
$$

with the fine structure constant $\alpha_{ls} \approx 1/137$, the orbital angular momentum $\boldsymbol{l}$, and the spin operator of the electron $\boldsymbol{s}$. This model potential has spherical symmetry and therefore conserves the total angular momentum $\boldsymbol{j}$=$\boldsymbol{l}$+$\boldsymbol{s}$. This permits the electronic wave function to be expanded as in [19]

$$
\begin{aligned}
|\psi_{ljm_j}\rangle &= R_{l,j}(r)\,|l,j,m_j\rangle \qquad (2.1)\\
\text{with} \quad |l,j,m_j\rangle &= \sum_{m_s=\pm 1/2} \langle l,1/2,m_l,m_s|j,m_j\rangle\,|l,m_l\rangle\,|s,s_z\rangle \quad .
\end{aligned}
$$

Here, $R_{l,j}(r)$ is the radial wave function and $|l,j,m_j\rangle$ represents the two-component spinor basis vector, with m_j (m_l) as the projection of j (l) onto the quantization axis. The expression $\langle l,1/2,m_l,m_j - m_l|j,m_j\rangle$ denotes the Clebsch-Gordan coefficients.

The low-lying electronic energies, calculated by Weibin Li with this model potential, are in good agreement with experimental values[3]. Therefore, the obtained electronic wave functions form a solid basis for the upcoming theoretical description and analysis of Rydberg states. A selection of the most significant electronic wave functions for us is shown in Fig. 2.2.

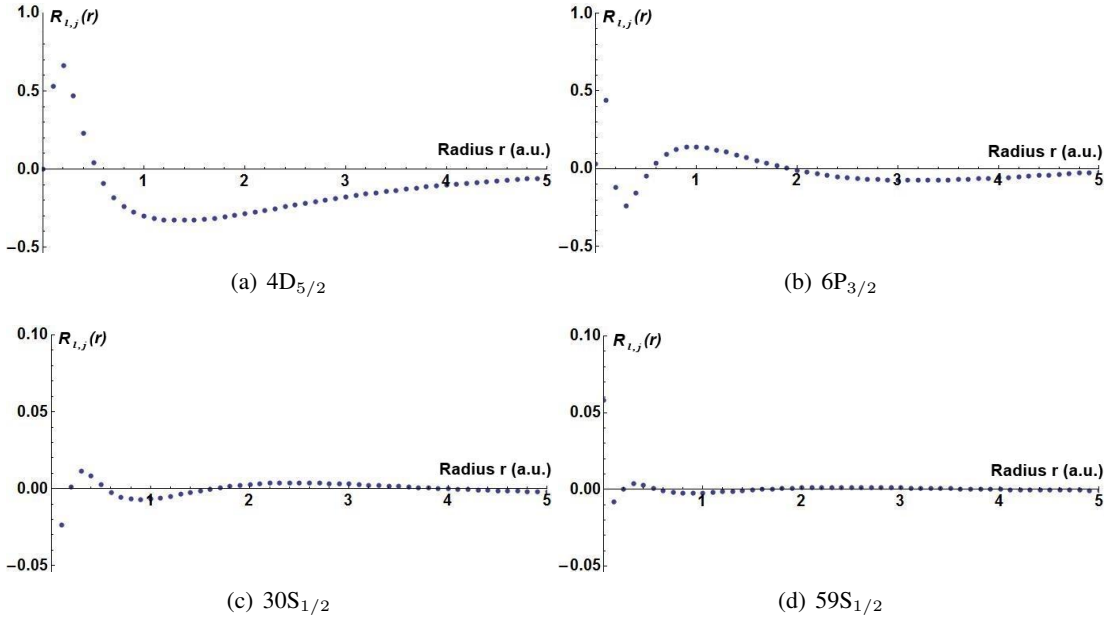

(a) $4D_{5/2}$ (b) $6P_{3/2}$

(c) $30S_{1/2}$ (d) $59S_{1/2}$

Figure 2.2: Theoretical electronic radial wave functions for the strontium ion as calculated by Weibin Li, University of Nottingham. The most relevant levels in the Rydberg excitation process are shown: $4D_{5/2}$, $6P_{3/2}$, and two Rydberg levels $30S_{1/2}$, and $59S_{1/2}$.

For the low-level states (a),(b) in Fig. 2.2 the probability density of the electron position is high near the ion core (small values r). However, for the Rydberg states (c),(d) the density at small r is much lower (note the different amplitude scaling) - it is spread over a larger radial distance from the core (Fig. 2.3). The expectation values for the position of the valence electron, $\langle\hat{r}\rangle$, represent this difference:

$$\langle\hat{r}\rangle = \langle\Psi_{l,j,m_j}|\hat{r}|\Psi_{l,j,m_j}\rangle = \int_0^\infty R^*_{l,j}\, R_{l,j}\, r^2\, dr \approx \begin{cases} 3 \text{ a.u.} & \text{for } 4D_{5/2} \\ 559 \text{ a.u.} & \text{for } 30S_{1/2} \end{cases},$$

Here, $|\Psi_{l,j,m_j}\rangle$ and $R_{j,l}$ are the full and the radial electronic wave functions (as in Eq. (2.1)), respectively, and $\hat{r}$ is the radial position operator.

[3] e.g. level energies in a.u. of $4D_{5/2}$: Experiment (NIST): -0.337752 / Weibin Li: -0.3376959 / other theory [20]: -0.337939

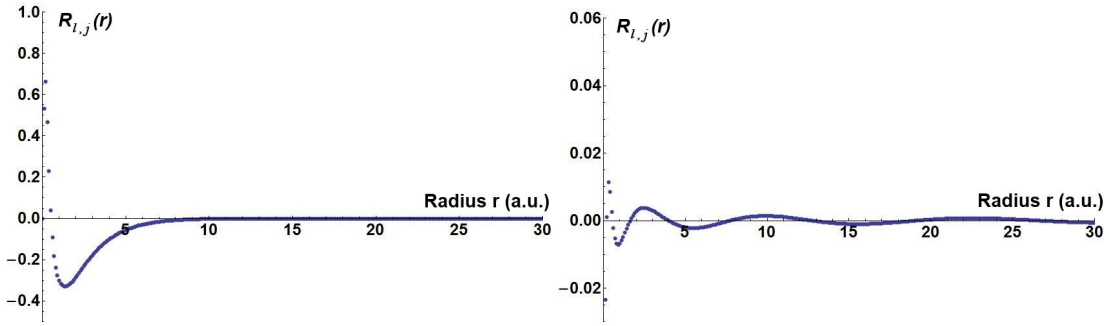

(a) $4D_{5/2}$ (b) $30S_{1/2}$

Figure 2.3: Theoretical electronic radial wave functions for the strontium ion. Graphs (a) and (d) of Fig. 2.2 are shown over a larger distance range. For the low-lying $4D_{5/2}$ level the probability density of the electron position is large around the ionic core, whereas for the Rydberg level $30S_{1/2}$ it is distributed over a large range.

The lifetime τ of a state i is given by $\tau = 1/A_i^{tot}$, where the total decay rate A_i^{tot} is the sum over all possible decay channels, respecting the selection rules $\Delta l = \pm 1$ and $\Delta m = 0, \pm 1$ [21]:

$$A_i^{tot} = \frac{e^2 w_{i\text{-}f}^3}{3\epsilon_0 \hbar c^3 \pi} \cdot |\langle i|\hat{r}|f\rangle|^2 \cdot \frac{\text{Max}[l_i, l_f]}{2l_i + 1} \quad ,$$

where $w_{i\text{-}f}$ is the frequency of the spontaneously emitted photon at the transition from the initial state i to a lower level f, for which $|l_i - l_f| = 1$ must be fulfilled. Note that the last term contains the angular part and accounts for the selection rule $\Delta m = 0, \pm 1$, whereas the dipole matrix element $\langle i|e \cdot \hat{r}|f\rangle$ is restricted to its radial part. Fig. 2.4 shows theoretically calculated lifetimes for S, D, and P Rydberg states with $n = 34 - 61$. The lifetimes τ are proportional to n^3, with n as the principal quantum number:

State	$\tau(n)$ in µs	State	$\tau(n)$ in µs
$S_{1/2}$	$2.9532 \cdot 10^{-5}\ n^{3.16957}$	$P_{1/2}$	$9.01022 \cdot 10^{-4}\ n^{3.08672}$
$D_{3/2}$	$4.1862 \cdot 10^{-5}\ n^{3.08935}$	$P_{3/2}$	$1.03304 \cdot 10^{-3}\ n^{3.09492}$
$D_{5/2}$	$4.3476 \cdot 10^{-5}\ n^{3.08943}$		

Table 2.2: Lifetime dependency on the principal quantum number n for S, D, and P Rydberg states with $n = 34 - 61$. Calculation by Weibin Li.

One notices that the P states live longer, making them potentially more useful for obtaining coherent Rydberg-Rydberg interactions. However, our planned two-photon excitation scheme employs the intermediate $6P_{3/2}$ level, from which only $S_{1/2}$, $D_{3/2}$, and $D_{5/2}$ are accessible.

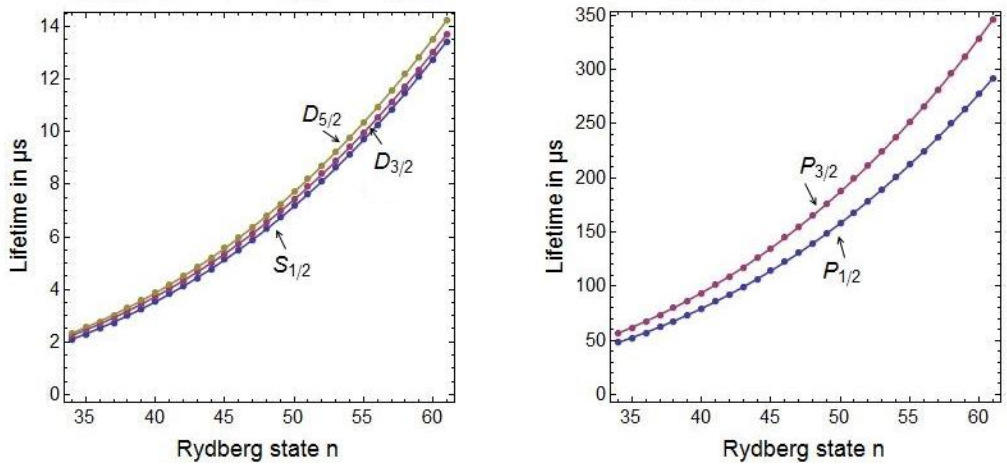

Figure 2.4: Lifetimes for S,D, and P Rydberg states, with principal quantum numbers n between 34 and 61. The P states live more than one order of magnitude ($\approx$ factor of 20) longer. The lifetimes are proportional to n^3, where the full fitting curves are specified in Tab. 2.2. Calculation by Weibin Li .

2.1.2 Rabi frequencies and linewidths

The Rabi frequency Ω of an electronic transition is given by the scalar product of the driving electric field strength $\mathbf{E_0}$ and the dipole matrix element of the transition $\hat{\mathbf{d}}_{\text{if}} = \langle i| -e\,\hat{\mathbf{r}}\,|f\rangle$. Here, $|i\rangle$ and $|f\rangle$ correspond to the calculated electronic wave functions of Eq. (2.1) for the initial and the final level, respectively. These wave functions generally depend on the quantum numbers n, j, m_j. Therefore, the dipole matrix element, and thus the Rabi frequency, varies with the respective initial and final states, accounting for the different transition probabilities.

$$\Omega = \frac{|\hat{\mathbf{d}}_{\text{if}} \cdot \mathbf{E_0}|}{\hbar} \tag{2.2}$$

For the two-step excitation into Rydberg levels we get:

$$\begin{aligned} &\text{step 1: } 4\text{D}_{5/2} \rightarrow 6\text{P}_{3/2}: \quad \lambda = 243 \text{ nm}\,,\ \Omega_1 = 2\pi\ 230 \text{ MHz} \\ &\text{step 2: } \begin{cases} 6\text{P}_{3/2} \rightarrow 30\text{D}_{5/2}: & \lambda = 309 \text{ nm}\,,\ \Omega_2 = 2\pi\ 117 \text{ MHz} \\ 6\text{P}_{3/2} \rightarrow 59\text{D}_{3/2}: & \lambda = 305 \text{ nm}\,,\ \Omega_2 = 2\pi\ 13 \text{ MHz} \end{cases} \end{aligned} \tag{2.3}$$

where we assume a laser power of 5 mW and a beam waist of 5 µm, which corresponds to focusing each laser down to a single ion[4]. Note that we selected the two radial target states with the lowest and highest wave function overlaps with the intermediate $6\text{P}_{3/2}$ state. This way we know over which range the Rabi frequencies are spread and we can estimate the critical values for other parameters, such as laser linewidths. Our two-photon excitation scheme can be

[4]The typical ion-ion distance in a linear Paul trap measures 5-10 µm. A beam waist of 5 µm allows individual ion addressing when the laser beam is perpendicular to the ion string. Considering the numerical aperture of the endcap electrodes in our trap, it is also possible to send the laser beam through the holes in the endcaps and to focus the laser to a spot size of 5 µm. This way the laser light propagates along the z-axis of the trap to address all ions simultaneously.

described by a three-level system with resonant two-photon excitation, where the driving lasers to and from the intermediate level are both detuned by the same value Δ (Fig. 2.5).

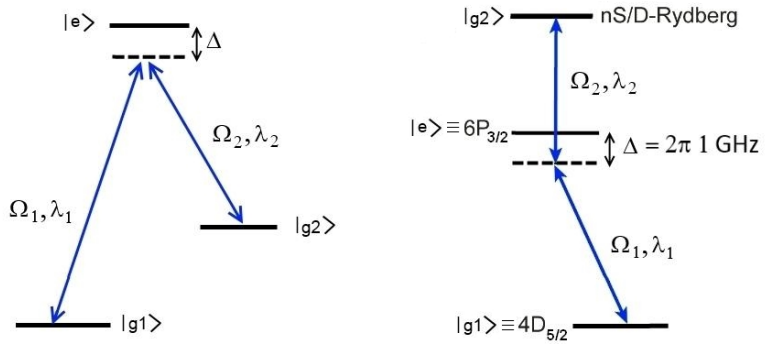

Figure 2.5: Our planned two-photon Rydberg excitation scheme (right) corresponds to a three-level system with two-photon resonance (left). The electron is excited from $4D_{5/2} \equiv |g1\rangle$ to a S/D Rydberg level $\equiv |g2\rangle$ without populating the intermediate state $|e\rangle \equiv 6P_{3/2}$. Δ: detuning, Ω_i: Rabi frequencies, λ_i: wavelengths.

The Hamiltonian for such a system in the basis $\{|g1\rangle, |g2\rangle, |e\rangle\}$ is given by [13]

$$H(t) = \frac{\hbar}{2} \begin{pmatrix} 0 & 0 & \Omega_1(t) \\ 0 & 0 & \Omega_2(t) \\ \Omega_1^*(t) & \Omega_2^*(t) & 2\Delta \end{pmatrix} \quad .$$

Under the conditions that $|\Delta| \gg \sqrt{|\Omega_1(t)|^2 + |\Omega_2(t)|^2}$ and $|\Delta| \gg \Gamma_{\text{intermediate}}$ the population of the intermediate state is negligible (adiabatic elimination) and the system evolves to an effective two-level system with the Hamiltonian [13]

$$H_{\text{eff}}(t) = \frac{\hbar}{2} \begin{pmatrix} -\frac{|\Omega_1(t)|^2}{2\Delta} & -\frac{\Omega_1(t)\Omega_2^*(t)}{2\Delta} \\ -\frac{\Omega_1^*(t)\Omega_2(t)}{2\Delta} & -\frac{|\Omega_2(t)|^2}{2\Delta} \end{pmatrix} \quad .$$

The effective Rabi frequency Ω_{eff} of our Rydberg excitation scheme is now given by the off-diagonal elements of the effective Hamiltonian

$$\Omega_{\text{eff}} = -\frac{\Omega_1 \Omega_2}{2\Delta} \quad , \tag{2.4}$$

while the diagonal elements lead to a light shift of the two levels which can be compensated by a respective two-level detuning. With a detuning of $\Delta = 2\pi$ 1 GHz, and Ω_1 and Ω_2 specified above, Ω_{eff} lies between 2π 1.5 MHz and 2π 13 MHz.
The following conditions must be fulfilled to drive the Rydberg transitions coherently:

1. $\Omega_{\text{eff}} \gg \Gamma$: The effective Rabi frequency has to be much larger than the linewidth of the addressed energy level $\Gamma = 1/\tau$. This way excitation and de-excitation can succeed before a spontaneous emission occurs. This condition is fulfilled for the S/D Rydberg levels of interest, which have lifetimes τ in the order of microseconds.

2. $\Delta\nu \ll \Omega_{\text{eff}}$: The linewidth $\Delta\nu$ of the transition driving lasers has to be much smaller than the Rabi frequency so that the phases of excitation and de-excitation coincide. Therefore, we want to achieve laser linewidths of $\Delta\nu \lesssim 100$ kHz.

This value for $\Delta\nu$ also allows individual level addressing: the energy difference between neighbouring levels is much bigger than the linewidths of the states[5]. So, with a linewidth of $\Delta\nu \sim 100$ kHz, Rydberg levels between $n = 30 - 60$ should be individually addressable.

2.2 Nonlinear optics

A weak light field interacting with a material system induces a polarization $P(t) = \chi^{(1)}E(t)$, which depends linearly upon the electric field strength $E(t)$. The proportionality factor $\chi^{(1)}$ is known as the linear susceptibility and describes phenomena in linear optics. Nonlinear optics, however, describes phenomena that occur when sufficiently intense light (typically laser light) interacts with an optical medium. The expression "nonlinear" refers to the nonlinear dependency of the material response upon the strength of the applied optical field [22]. In contrary to the linear case, the polarization also depends on quadratic and higher order terms of $E(t)$. So $P(t)$ can be expressed as a power series in the electrical field strength:

$$\begin{aligned} P(t) &= \chi^{(1)}E(t) + \chi^{(2)}E^2(t) + \chi^{(3)}E^3(t) + ... \\ &\equiv P^{(1)}(t) + P^{(2)}(t) + P^{(3)}(t) + ... \quad , \end{aligned} \tag{2.5}$$

where $\chi^{(2)}$ and $\chi^{(3)}$ denote the second- and third-order nonlinear optical susceptibilities, respectively. In the most general case, the fields $P(t)$ and $E(t)$ are represented by vectors and the susceptibilities are tensors of the correspondent rank. Nonlinear optical interactions of the second order (described by $\chi^{(2)}$) can only occur in non centrosymmetric crystals (e.g. barium borate (BBO), lithium triborate (LBO), lithium niobate (LN)). Liquids, gases, amorphous solids and many crystals show inversion symmetry, for which $\chi^{(2)}$ vanishes. Each atom in the material sample, which feels an incident field, develops an oscillating dipole moment. Every oscillating dipole is a source for new electromagnetic field components, even with different frequencies in the nonlinear case (as discussed below, e.g. in Eq. (2.6) and (2.7)). The phase velocity[6] of an electromagnetic wave depends on the refractive index of the traversed medium, which changes with frequency. Therefore, the velocity of the incident, polarizing wave can differ from the internal radiated field components. This causes dephasing of the single newly generated waves radiated off the individual dipoles and results in alternating areas of constructive and destructive interference along the entire propagation length. As explained in subsection 2.2.2, a proper relative phasing of the single dipoles can be achieved via special techniques, so called "phase matching" methods.

Nonlinear optical processes can be used to convert laser light of commercially obtainable frequencies into special and not directly available frequencies. This method will be used for producing the UV laser light for the Rydberg excitation (243 nm and 304-310 nm), specifically two second-order nonlinear effects are employed; Second-Harmonic Generation (SHG) and the Sum-Frequency Generation (SFG), both described in the following subsection.

[5] Example of one of the smallest energy level differences $60D_{5/2} \leftrightarrow 60D_{3/2}$: Energy difference $\Delta E = h \cdot$ 77 MHz, linewidth of the $60D_{5/2}$ $\tau = 13.5\ \mu s \Rightarrow \Gamma = 73.8$ kHz.

[6] The phase or propagation velocity is the speed at which the phase of a wave propagates through space. In contrary, the group velocity is the speed of the wave-packet propagation, carrying the information.

2.2.1 Second-harmonic generation and sum-frequency generation

As explained in 2.1, for the two Rydberg excitation steps special UV laser sources are required. 243 nm light is obtained by frequency quadrupling (two successive SHGs) of a 972 nm diode laser. 607-619 nm light is generated by a sum-frequency process with 1551 nm and tunable 1000 nm light and then sent through another frequency doubling unit, in order to produce 304-310 nm. The principles behind this nonlinear effects are described in the following.

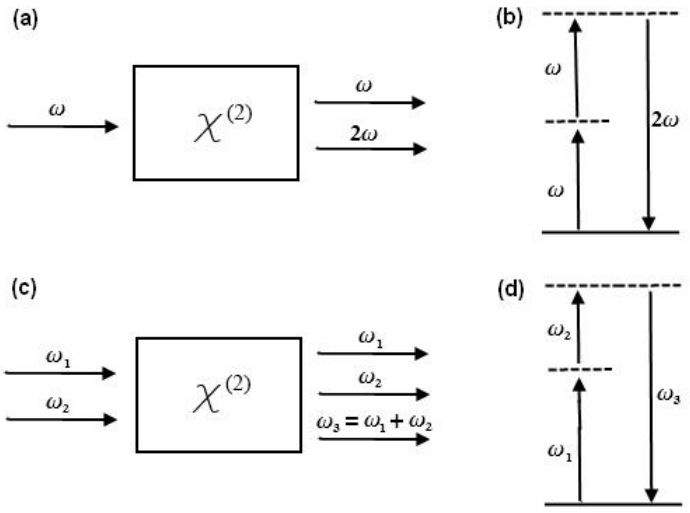

Figure 2.6: The schematics (a) and (c) show the interaction geometry of second-harmonic generation and sum-frequency generation, respectively, illustrating the generation of new frequency components in the radiated field. (b) and (d) are energy-level diagrams which describe the SHG and SFG process. Two photons are annihilated while one photon with doubled (respectively summed) frequency is produced.

In **second-harmonic generation** a laser beam with frequency w is incident upon a nonlinear crystal (for which $\chi^{(2)}$ is non-zero). Since the electric field strength is given as $E(t) = E_0 \cdot e^{-iwt} + c.c.$ the created second-order nonlinear polarization can be written as

$$P^{(2)}(t) = \chi^{(2)} E^2(t) = 2\chi^{(2)} E_0 E_0^* + \left(\chi^{(2)} E_0^2 \cdot e^{-2iwt} + c.c.\right) \quad . \tag{2.6}$$

The polarization has one component at zero frequency[7] and one at frequency $2w$. The latter one leads to radiation at the so called "second-harmonic frequency" $2w$. To visualize this process one can consider it as energy exchange between different frequency components of the field. Part (a) and (b) of Fig. 2.6 demonstrate this concept where a laser field of frequency w is converted to a field with components w and $2w$ (we can neglect the low radiation intensity of higher order terms). In other words: two photons of frequency w are annihilated and at the same time a photon of frequency $2w$ is created.

In the case of **sum-frequency generation** the incident optical field consists of two different frequency components and can be expressed as $E(t) = E_1 \cdot e^{-iw_1 t} + E_2 \cdot e^{-iw_2 t} + c.c.$. Sub-

[7] The contribution at zero frequency does not lead to electromagnetic radiation but leads to "optical rectification": a static electric field appears in the nonlinear crystal.

stituting this into Eq. (2.5), the second-order contribution to the nonlinear polarization is given by

$$\begin{aligned} P^{(2)}(t) = &\chi^{(2)} E^2(t) = \chi^{(2)} \Big[E_1^2 \cdot e^{-2iw_1 t} + E_2^2 \cdot e^{-2iw_2 t} + 2E_1 E_2 \cdot e^{-i(w_1+w_2)t} \\ &+ 2E_1 E_2^* \cdot e^{-i(w_1-w_2)t} + c.c. \Big] + 2\chi^{(2)} \left[E_1 E_1^* + E_2 E_2^* \right] \quad . \end{aligned} \tag{2.7}$$

This formula has contributions at zero, double-, sum- and difference-frequencies, each of which representing a different nonlinear optical process: optical rectification (zero freq.), second-harmonic generation (doubled frequencies $2w_1$ and $2w_2$), sum-frequency generation ($w_1 + w_2$) and difference-frequency generation ($w_1 - w_2$ and $w_2 - w_1$). Nevertheless, in practice only one of the possible frequency components is produced at a significant radiation intensity. This is due to the fact that usually only one frequency component satisfies the phase matching condition required for efficient generation of an electromagnetic signal. By properly adjusting some external conditions (see subsection 2.2.2 for details) one can choose the process which will be phase matched and the corresponding frequency component will then be radiated. The phase matching condition is related to momentum conservation and is written as $\hbar k_3 = \hbar k_1 + \hbar k_2$ (for the example of SFG). Additionally, energy conservation must be fulfilled: $\hbar w_3 = \hbar w_1 + \hbar w_2$. Diagrams (c) and (d) in Fig. 2.6 show the interaction scheme and a virtual energy-level diagram of SFG. It becomes clear that second-harmonic generation corresponds to a special case of sum-frequency generation with $w_1 = w_2 = w$.

2.2.2 Coupled wave equations and phase matching

By describing the nonlinear interaction with Maxwell's equations one can theoretically examine how the nonlinear polarization develops and how the different frequency components of the electromagnetic field interact with each other. This also explains the development of domains of constructive and destructive interference and the principle of phase matching. For simplicity, the following formulas are given in the Gaussian CGS-system[8]. At first, the nonlinear polarization $\mathbf{P}$ is added as a source term in Maxwell's equations [22, 23]:

$$\nabla \times \mathbf{E} = -\frac{1}{c}\frac{\partial \mathbf{B}}{\partial t} \tag{2.8}$$

$$\nabla \times \mathbf{B} = \frac{1}{c}\frac{\partial \mathbf{D}}{\partial t} \tag{2.9}$$

$$\text{with} \quad \mathbf{D} = \epsilon \mathbf{E} + 4\pi \mathbf{P} \tag{2.10}$$

Here, it is assumed that the material is non-magnetic ($\mathbf{B} = \mathbf{H}$) and that no free charges or free currents appear ($\rho = 0$, $\mathbf{J} = 0$). The linear polarization is included in the dielectric tensor[9] ϵ and $\mathbf{P}$ denotes the nonlinear polarization only. Taking the curl of both sides in Eq. (2.8) and combining the three equations (2.8), (2.9) and (2.10) one obtains

$$\nabla \times \nabla \times \mathbf{E} = -\frac{\epsilon}{c^2}\frac{\partial^2 \mathbf{E}}{\partial t^2} - \frac{4\pi}{c^2}\frac{\partial^2 \mathbf{P}}{\partial t^2} \quad .$$

[8] Electric field strength: $E^{CGS} = \sqrt{4\pi\epsilon_0} \cdot E^{SI}$, electric displacement field: $D^{CGS} = \sqrt{4\pi/\epsilon_0} \cdot D^{SI}$, magnetic field strength: $B^{CGS} = \sqrt{4\pi/\mu_0} \cdot B^{SI}$, magnetizing field strength: $H^{CGS} = \sqrt{4\pi\mu_0} \cdot H^{SI}$, $c^2 = \frac{1}{\epsilon_0 \mu_0}$

[9] For simplicity it is assumed to have an isotropic material for which ϵ reduces to a scalar.

This is the basic wave equation in nonlinear optics. By substituting $\nabla \times \nabla \times \mathbf{E} = \nabla(\nabla \cdot \mathbf{E}) - \nabla^2\mathbf{E}$ and neglecting[10] the first term on the right-hand side, the equation transforms to

$$\nabla^2\mathbf{E} = \frac{\epsilon}{c^2}\frac{\partial^2\mathbf{E}}{\partial t^2} + \frac{4\pi}{c^2}\frac{\partial^2\mathbf{P}}{\partial t^2} \quad . \tag{2.11}$$

We want to use this equation on the example of sum-frequency generation, where three interacting monochromatic continuous-waves travel through a nonlinear optical medium. Moreover, we assume that the waves propagate in z direction, thus we restrict the problem to only one dimension. For this case the applied fields are given by

$$\begin{aligned} E_1(z,t) &= A_1 e^{i(k_1 z - w_1 t)} \\ E_2(z,t) &= A_2 e^{i(k_2 z - w_2 t)} \\ E_3(z,t) &= A_3 e^{i(k_3 z - w_3 t)} \end{aligned} \tag{2.12}$$

with similar equations for the complex conjugates. The field amplitudes A_i are slowly varying functions in z and the three frequencies are connected by $w_3 = w_1 + w_2$. According to [22] (Sec. 1.5) the determining polarization term P_3 can be written as

$$P_3(z,t) = 4dA_1A_2e^{i[(k_1+k_2)z - w_3 t]} \quad , \tag{2.13}$$

where the coupling coefficient d arises from the effective nonlinear susceptibility. We insert Eq. (2.12) and Eq. (2.13) into the wave equation (2.11), to see how the field component E_3 with sum-frequency w_3 develops.

$$\text{left side:} \quad \frac{\partial^2 E_3}{\partial z^2} \rightarrow \left(\frac{d^2A_3}{dz^2} + 2ik_3\frac{dA_3}{dz} - k_3^2 A_3\right) e^{i(k_3 z - w_3 t)}$$

$$\text{right side:} \quad \frac{\epsilon}{c^2}\frac{\partial^2 E_3}{\partial t^2} + \frac{4\pi}{c^2}\frac{\partial^2 P_3}{\partial t^2} \rightarrow -\frac{\epsilon w_3^2}{c^2}A_3 e^{i(k_3 z - w_3 t)} - \frac{16\pi d w_3^2}{c^2}A_1A_2e^{i[(k_1+k_2)z - w_3 t]}$$

Using $\epsilon_{(w_3)} = n_3^2$ and the dispersion relation $k_3 = n_3 w_3/c$ the third term of the left side cancels with the first term of the right side. Additionally, $e^{-iw_3 t}$ cancels on both sides and one gets

$$\frac{d^2A_3}{dz^2} + 2ik_3\frac{dA_3}{dz} = -\frac{16\pi d w_3^2}{c^2}A_1A_2e^{i(k_1+k2-k_3)z} \quad .$$

If the slowly-varying amplitude approximation[10] is applied again, $\frac{d^2A_3}{dz^2}$ can be neglected. With the so called **wave vector mismatch** $\Delta k = k_1 + k_2 - k_3$ one finally obtains

$$\frac{dA_3}{dz} = \frac{8\pi i d w_3^2}{k_3 c^2}A_1A_2e^{i\Delta k z} \quad . \tag{2.14}$$

Eq. (2.14) shows the coupling between the three appearing waves w_1, w_2, w_3 and in particular how the amplitude of w_3 depends on the other two. Thus, it is called a **coupled-amplitude equation**. Analogously one can derive equivalent equations for the other two fields:

$$\begin{aligned} \frac{dA_1}{dz} &= \frac{8\pi i d w_1^2}{k_1 c^2}A_3A_2^*e^{-i\Delta k z} \\ \frac{dA_2}{dz} &= \frac{8\pi i d w_2^2}{k_2 c^2}A_3A_1^*e^{-i\Delta k z} \end{aligned}$$

[10] Valid for example if the incident field $\mathbf{E}$ has the form of a transverse, infinite plane wave (for which $\nabla\mathbf{E} = 0$), or more generally in the slowly varying amplitude approximation, if $\left|\frac{d^2E}{dz^2}\right| \ll \left|k_i\frac{dE}{dz}\right|$.

Assuming that the conversion of the incoming fields into the generated sum-frequency field is small, the amplitudes A_1 and A_2 are constant. In this case, the three coupled-amplitude equations reduce to one which is quite easy to integrate along the entire propagation path (for example, a crystal with length L). So the amplitude of the field E_3 at the end of the crystal is given by

$$A_3(L) = \frac{8\pi i d w_3^2}{k_3 c^2} A_1 A_2 \int_0^L e^{i\Delta k z} dz = \frac{8\pi i d w_3^2}{k_3 c^2} A_1 A_2 \left(\frac{e^{i\Delta k L} - 1}{i\Delta k} \right) \quad . \tag{2.15}$$

The intensity of the sum-frequency field is given by the power per unit area (time averaged Poynting vector) which is defined by [22]

$$\begin{aligned} I_3 &= \frac{n_3 c}{2\pi} |A_3|^2 \\ &= \frac{n_3 32\pi d^2 w_3^4 |A_1|^2 |A_2|^2}{k_3^2 c^3} \left| \frac{e^{i\Delta k L} - 1}{\Delta k} \right|^2 \quad . \end{aligned} \tag{2.16}$$

Finally, we substitute $\left| \frac{e^{i\Delta k L} - 1}{\Delta k} \right|^2 = L^2 \mathrm{sinc}^2(\Delta k \frac{L}{2})$, $k_3 = \frac{n_3 w_3}{c}$, $w_3 = \frac{2\pi c}{\lambda_3}$ and express $|A_1|^2$ and $|A_2|^2$ in terms of their intensities according to Eq. (2.16):

$$^{(11)} I_3 = \frac{512\pi^5 d^2 I_1 I_2}{n_1 n_2 n_3 c \lambda_3^2} L^2 \mathrm{sinc}^2 \left(\frac{\Delta k L}{2} \right) \tag{2.17}$$

At this point, an intuitive explanation for this signal shape should be considered: In Eq. (2.15) one integrates over all wave-contributions (of the form e^{ikz}) arising along the propagation path z of the polarizing wave. This corresponds to a Fourier transformation of a step function between 0 and L which results in the sinc-function of Eq. (2.17).

The sinc-factor depends on the wave vector mismatch and the length of the nonlinear material. So the efficiency of sum-frequency generation generally decreases with increasing $|\Delta k| L$, with some additional oscillations (see Fig. 2.7). This is because when L is bigger than $\pi/\Delta k$ the generated electromagnetic wave runs out of phase with its driving polarization wave, they interfere destructively and the output power decreases. At the coherence length $L_c = 2\pi/\Delta k$ the intensity of the generated field vanishes completely.

[11] Note that the calculation was performed in the CGS-system, which means that conversion factors have to be taken into account, to get the right physical values. Nevertheless, this equation is only a theoretical simplification, in order to see the dependency of the output power on the incident light intensities and the phase mismatch. A more realistic, physical formula is given by Eq. (3.3), which additionally contains contributions of absorption, phase mismatch, focusing parameters, and double refraction.

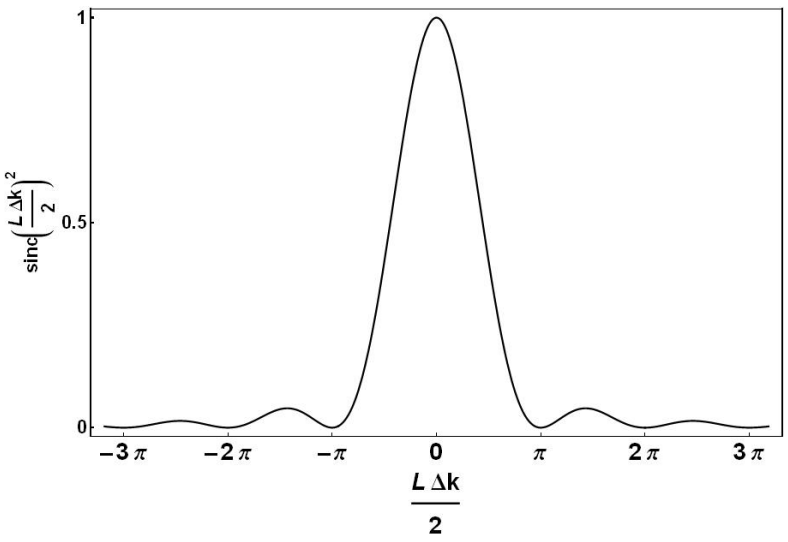

Figure 2.7: Efficiency of sum-frequency generation as a function of the wave vector mismatch.

In summary one distinguishes between two cases:

1. If $\Delta k \neq 0$ the output intensity varies with the length of the crystal in a $(\mathrm{sinc})^2$ fashion.

2. The condition $\Delta k = 0$ or $k_3 = k_1 + k_2$ is known as perfect phase matching. In this case the individual atomic dipoles are properly phased so that the newly generated waves interfere constructively and add together coherently. Therefore, frequency conversion is maximally efficient. From Eq. (2.17) the intensity of the sum-frequency wave is then proportional to the power of the input intensities and to the square of the crystal length.

Phase matching considerations

The condition of phase matching between the polarizing and generated waves can be reached by several approaches. The following pages present two methods by which we achieve phase matching [23, 24]: a technique to obtain true phase matching and a quasi-phase matching method. These approaches are explained on the example of second-harmonic generation, which involves waves of only two different frequencies and therefore simplifies the description.

The technique of **angle phase matching** was published in 1962 by Giordmaine [25] and, independently, by Terhune and co-workers [26]. The wave vector mismatch results from the difference between the velocities of the fundamental wave $c_1(w)$ and the second-harmonic $c_2(2w)$. This difference is caused by the unequal frequencies and therefore differing refractive indices of the two waves ($c_i = c_{vac}/n_i$). The basic idea of angle phase matching is to match the refractive indices by employing the birefringence of a uniaxial crystal. Such a crystal is defined by two refractive indices, the ordinary n_o and the extraordinary n_e. Let us assume that the electric field of our incident fundamental beam w is polarized perpendicular to the optical axis of the crystal and forms the so called ordinary ray, whose refractive index $n_o(w)$ is independent of the angle of incidence. The generated second-harmonic $2w$ is then polarized parallel[12] to the optical axis

[12] A polarizing electric field of the form $E_i = (E_i^x, E_i^y, 0)$ generates a field perpendicular to it $E_f = (0, 0, E_f^z)$, due to the tensor properties of the second-order susceptibility $\chi^{(2)}$.

and forms the extraordinary ray for which the index $n_e^{2w}(\theta)$ changes as function of the angle of incidence θ with respect to the optical axis (Eq. (2.18)). The change proceeds in form of an elliptic function between the value of the ordinary index $n_o(2w)$ and the extraordinary index $n_e(2w)$. Consequently, one will choose[13] the angle in such a way that the indices of the fundamental and the second-harmonic wave are matched $n_e^{2w}(\theta) \equiv n_o(w)$ and therefore the phase matching condition is fulfilled (Fig. 2.8).

$$n_e^{2w}(\theta) = \frac{n_e(2w) \cdot n_o(2w)}{[(n_o(2w))^2 \cdot sin^2(\theta) + (n_e(2w))^2 \cdot cos^2(\theta)]^{1/2}} \equiv n_o(w) \tag{2.18}$$

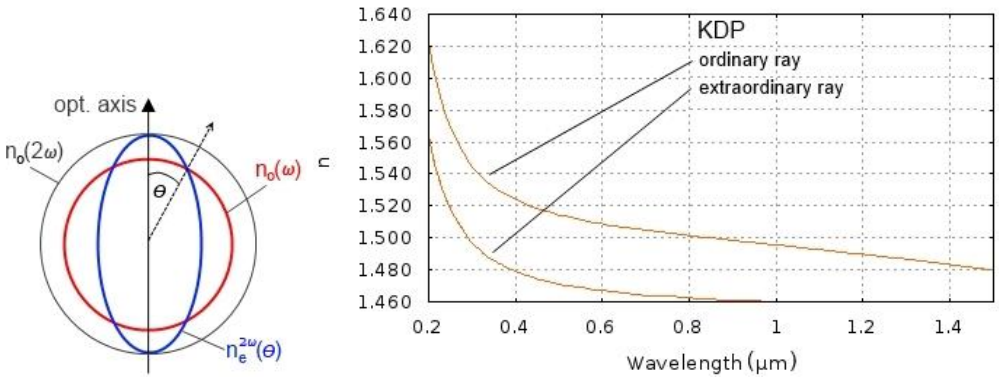

(a) (b)

Figure 2.8: (a) Dependence of ordinary and extraordinary indices on the angle of incidence θ for a KDP crystal. Since the crystal is uniaxial birefringent the function shows rotation symmetry around the optical axis. The red circle denotes the angle-independent, ordinary index of the fundamental $n_o(w)$, the blue ellipse shows the extraordinary index of the second-harmonic $n_e^{2w}(\theta)$, which is dependent on the angle of incidence. At a certain angle θ the two indices are equal. (b) Dispersion in the negative uniaxial KDP [27, 28]. The ordinary index is always larger than the extraordinary which means that angle phase matching is possible only if the fundamental waves propagate as ordinary rays.

Depending on the type of uniaxial crystal the fundamental beam has to be applied either as ordinary or as extraordinary ray: for negative uniaxial crystals (Fig. 2.8(b)) the ordinary index is larger than the extraordinary index $n_o > n_e$, for which reason[14] one chooses the fundamental wave propagating as ordinary ray (electric field polarized perpendicular to the optical axis). For positive uniaxial crystals it is the opposite and one uses an extraordinary fundamental. This type of phase matching is called *type I phase matching*. In *type II phase matching* the fundamental wave is in a superposition of horizontal and vertical polarization. The second-harmonic is generated by mixing the ordinary and the extraordinary component of the fundamental beam.

[13] Example with KDP (potassium dihydrogen phosphate) as negative, uniaxial crystal, for a fundamental beam of $\lambda_f = 610$ nm and a second-harmonic of $\lambda_{SH} = 305$ nm: According to [27] the refractive indices are $n_o(w) = 1.5084$, $n_o(2w) = 1.54345$, $n_e(2w) = 1.49629$. With these values Eq. (2.18) solves for $\theta \approx 59°$.

[14] From the example in footnote[13], i.e. for normal dispersion where $n(2w) > n(w)$, one sees that only in this case the target index $n_o(w)$ lies within the given index-range for $n_e^{2w}(\theta)$: $[n_e(2w) - n_o(2w)]$.

Quasi-phase matching is another approach to avoid the dephasing of the polarizing and generated waves. Eq. (2.17) shows that the intensity of the generated field reaches its maximum at the so called coherence length $L_c = \pi/\Delta k$ from where it starts to decrease until it returns to zero at $L = 2L_c$. If the phase of the second-harmonic is changed by 180° at exactly the point where destructive interference starts, the phase mismatch can be partially compensated (therefore, QUASI-phase matching): the intensity generated after one coherence length of the quasi-phase matched crystal is smaller, by a factor[15] $4/\pi^2$, than the intensity from a perfectly phase matched crystal of the same length. One technique to realize this phase jump is to cut plates of the crystal with a thickness of one coherence length and stick them together so that every second plate is turned over (the rotation axis corresponds to the optical axis). This causes a change of sign of the nonlinear susceptibility and therefore a 180° phase change for the polarization wave. Fig. 2.9(a) illustrates this principle. The problem is that it can be very difficult to cut such thin plates from a crystal (the thickness is down to 5 µm). Another way to obtain periodically inverted crystals is by growing semiconductor layers epitaxially one on the other. Nevertheless, in the most commonly used technique today a static electric field is applied to ferroelectric crystals to induce a permanent electric polarization. A periodically poled field generates a corresponding poled crystal. In the sense of phase matching the periodicity, with period length $\Lambda = 2L_c$, acts as an additional k-vector $k_\Lambda = 2\pi/\Lambda$ which sets the wave vector mismatch Δk artificially to zero:

$$\Delta k \equiv 0 \Leftrightarrow k_3 = k_1 + k_2 + k_\Lambda \quad . \tag{2.19}$$

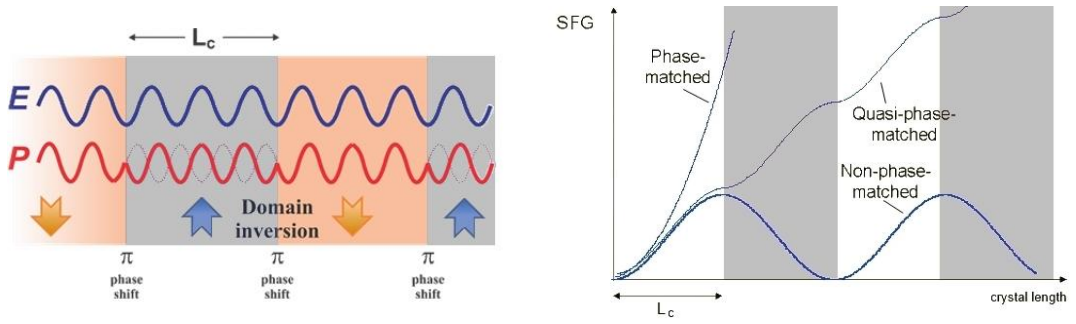

(a) (b)

Figure 2.9: (a) Principle of quasi-phase matching with a periodically poled crystal (c.f [29]). The electric field component of the fundamental wave (blue sine) propagates unaffected through the material, while the induced polarization wave of the second harmonic (red curve) changes by 180° after every multiple of the coherence length L_c. Thus the newly generated electric rays of the single domains interfere constructively. (b) SFG output signal for the cases of: no-phase matching, quasi-phase matching and perfect phase matching (c.f [30]). For perfect phase matching the signal would be proportional to the square of the crystal length. Instead of decreasing after one coherence length the signal in the quasi-phase matched case rises further and sets itself apart from the signal in a non-phase matched case which drops to zero after twice the coherence length.

[15] Regarding Eq. (2.17): $I_3 \propto sinc^2\left(\frac{\Delta k L}{2}\right) = \left(\frac{2}{\pi}\right)^2$ for $L = \pi/\Delta k$.

The advantage of quasi-phase matching over angle phase matching is that it can also be used with isotropic crystals. Besides, there is another problem in birefringent crystals: the direction of an extraordinary ray (which corresponds to the direction of the poynting vector) is only parallel to its wave vector (normal to the wave fronts), if the angle of incidence $\theta = 0°$ or $90°$. This means that in a phase-matched case, with an angle of incidence $0° < \theta < 90°$, the ordinary and the extraordinary beam diverge with increasing propagation path (*walk-off*) and thus do not overlap for the entire crystal length. Only the projection onto the polarizing electric field component accounts for the generation of the second-harmonic. So the output signal is not proportional to the square, but rather to a lower power of the crystal length. For quasi-phase matching, however, the angle θ can be chosen to be $\theta = 0°$ or $90°$ such that no walk-off occurs. An additional advantage of quasi-phase matching is that the orientation of the crystal, with respect to the incident waves, can often be chosen such that the $\chi^{(2)}$ is largest.

In the QuaSIRIO-project we make use of both methods discussed here. For the SHG angle-phase matching is employed, with lithium triobate (LBO) or barium borate (BBO) as the nonlinear crystals. For SFG we want to be able to tune the generated wavelength within several nanometres. For this reason a Periodically Poled Lithium Niobate (PPLN) crystal with 5 paths of different periodicities is used. By choosing a suitable path and the corresponding temperature, the entire range of required wavelengths can be achieved by phase matching (see Sec. 3.1).

Chapter 3

Technical principles

3.1 PPLN crystal and the Sellmeier equation

Quasi-phase matching adds an additional term to the equation of momentum conservation due to periodical poling of the nonlinear crystal. This poling, with period length Λ, adds an artificial k-vector $k_\Lambda = \frac{2\pi}{\Lambda}$ so that: $\Delta k \equiv 0 \Leftrightarrow k_3 = k_1 + k_2 + k_\Lambda$. This equation is equivalent to

$$\frac{n_e(\lambda_3, T)}{\lambda_3} = \frac{n_e(\lambda_1, T)}{\lambda_1} + \frac{n_e(\lambda_2, T)}{\lambda_2} + \frac{1}{\Lambda} \quad , \tag{3.1}$$

where n_e are the refractive indices for extraordinary polarized waves, T is the temperature of the nonlinear crystal, and $\lambda_{1/2/3}$ the wavelength of the respective propagating beam (here for example: $\lambda_1 = 1000$ nm, $\lambda_2 = 1551$ nm, $\lambda_3 = 608$ nm). The Sellmeier equation describes the dependence of the refractive index on the temperature of the medium and on the wavelength of the traversing beam [31]:

$$n_e^2(\lambda, f(T)) = a_1 + b_1 \cdot f + \frac{a_2 + b_2 \cdot f}{\lambda^2 - (a_3 + b_3 \cdot f)^2} + \frac{a_4 + b_4 \cdot f}{\lambda^2 - a_5^2} - a_6 \lambda^2 \quad . \tag{3.2}$$

The temperature T is included in the parameter $f = (T - T_0)\,(T + T_0 + 2 \cdot 273.16)$ with the reference temperature $T_0 = 24.5$ °C. The coefficients a_i and b_i account for different contributions [31–33] to the refractive index from: plasmons and poles in the UV and IR, thermal effects, multiphonon absorption, and optical anisotropies. Tab. 3.1 lists the Sellmeier coefficients for the nonlinear crystal used in our setup. Inserting (3.2) into (3.1) results in an extensive equation, describing the relation between temperature, poling period of the crystal, and wavelengths of the respective laser beams. This formula can be visualized by a graph as in Fig. 3.3.

a_1	5.756	a_6	$1.32 \cdot 10^{-2}$
a_2	0.0983	b_1	$2.860 \cdot 10^{-6}$
a_3	0.2020	b_2	$4.700 \cdot 10^{-8}$
a_4	189.32	b_3	$6.113 \cdot 10^{-8}$
a_5	12.52	b_4	$1.516 \cdot 10^{-4}$

Table 3.1: Sellmeier coefficients for 5% MgO-doped congruent $LiNbO_3$, according to Eq. (3.2) as given in [31].

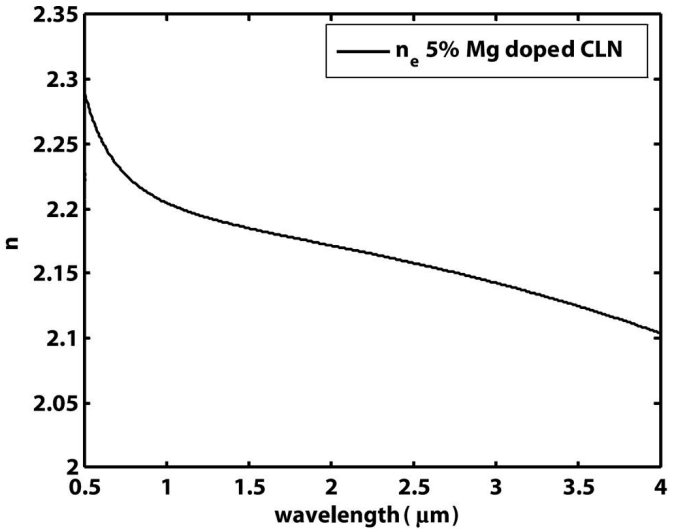

Figure 3.1: Extraordinary refractive index curve for 5% MgO doped congruent $LiNbO_3$ at room temperature, according to the Sellmeier coefficients given in Tab. 3.1. (c.f [31])

The nonlinear crystal in our setup is a 4 cm long, 0.5 mm thick, magnesium-doped congruent lithium niobate crystal (see Fig. 3.2), with five parallel gratings of different poling periodicities between $10.40\,\mu m$ and $11.00\,\mu m$. The single paths are 0.5 mm wide and separated by 0.2 mm wide areas of unpoled material. The device is etched in order to indicate the poled regions. The individual paths are represented in graph 3.3 by five phase matching curves, distinguished by color. The advantage of several periodicities in one crystal is that the phase matching condition can be satisfied for a broader range of wavelengths, with one and the same crystal. This feature ensures fast and simple tunability of the generated sum-frequency light: First, with the aid of graph 3.3, one finds the appropriate combination of periodicity and temperature for the desired wavelength. Temperatures above 100 °C are preferred because they prevent the crystal from photorefractive damage [34]. Secondly, the crystal position is shifted until the incident fundamentals propagate along the selected path. The gray area in Fig. 3.3 shows the region over which the 1000 nm fundamental laser is tuned (while the second fundamental is fixed at 1551 nm) to obtain laser light between 607-619 nm. Frequency-doubling of this light generates the 304-310 nm light, which is required for the planned excitation into Rydberg levels between $n = 30 - 60$ (Sec. 2.1).

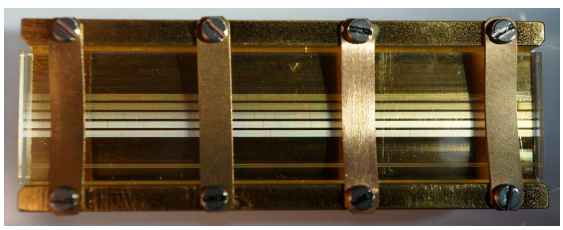

Figure 3.2: Photograph of the PPLN in a metal holder. The luminous stripes, running from the left to the right, indicate the five different periodicity gratings of the crystal.

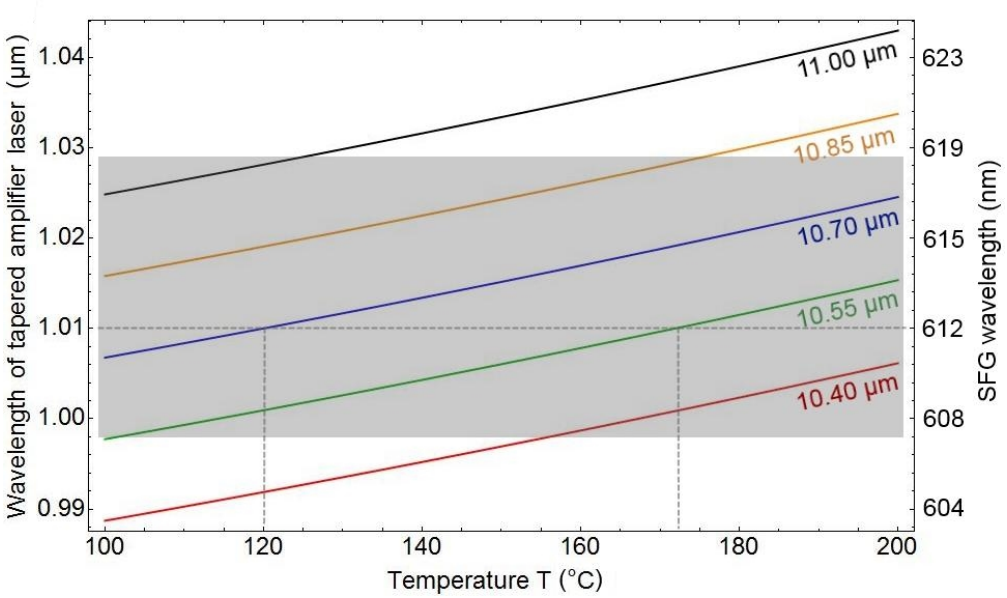

Figure 3.3: Theoretically calculated Sellmeier curves for a 5% MgO-doped congruent $LiNbO_3$ with five periodically poled gratings. The colors denote the different periodicities: $11.00\,\mu m$ (black), $10.85\,\mu m$ (yellow), $10.70\,\mu m$ (blue), $10.55\,\mu m$ (green), $10.40\,\mu m$ (red). The transparent gray area shows the region of interest for the Rydberg experiment: We fix the wavelength of the first fundamental at 1551 nm while the second fundamental is tuned between 998-1029 nm to generate 607-619 nm laser light by sum-frequency generation. For example: if we choose the wavelength of the second fundamental to be 1010 nm, the phase matching condition will be fulfilled for a temperature of ≈120 °C in the $10.70\,\mu m$ (blue) grating or for ≈175 °C in the $10.55\,\mu m$ (green) grating. The generated laser light will have a wavelength of 612 nm.

3.2 Optimized focusing into the nonlinear crystal

In 1968 Boyd and Kleinmann published a paper [35] in which the optimization of second-harmonic generation and parametric generation for Gaussian beams were studied. They found that the treatment of three-wave mixing processes (such as SFG) is formally identical to the theory of second-harmonic generation. The mixing power P_3 is derived to be

$$P_3 = K P_1 P_2 l k_0 e^{-\alpha' l} \cdot \left[(1-\zeta^2)(1-\gamma^2)/(1+\gamma\zeta)\right] \cdot h(\sigma,\beta,\kappa,\xi,\mu) \quad , \tag{3.3}$$

with a material constant K (containing refractive indices, wavelengths, and the nonlinear coefficient d), incident fundamental powers P_1 and P_2, and crystal length l. $\alpha' = 1/2(\alpha_1+\alpha_2+\alpha_3)$ contains the absorption coefficients $(\alpha_1,\alpha_2,\alpha_3)$) of the three interacting light fields. The parameters k_0, ζ and γ depend on the frequencies (w_1, w_2) of the fundamental light fields and the respective refractive indices (n_1, n_2):

$$k_0 = \frac{n_0 w_0/2}{c} \quad , \quad \gamma = \frac{w_2 - w_1}{w_2 + w_1} \quad , \quad \zeta = \frac{n_2 - n_1}{n_2 + n_1} \quad ,$$

where the variables $n_0 = (n_1+n_2)/2$ and $w_0 = (w_1+w_2)/2$ describe the degenerate refractive index and degenerate frequency, respectively. The function $h(\sigma,\beta,\kappa,\xi,\mu)$ generally depends

on all adjustable parameters required for the maximization of the output power of SFG: the phase mismatch σ, the focal position μ, the focusing strength ξ, the double refraction β, and the absorption κ:

$$\begin{aligned}\sigma &= z_R \cdot \Delta k \\ \xi &= \frac{l}{2 \cdot z_R} \\ \beta &= \frac{\rho}{\delta_0} \\ \kappa &= 1/2(\alpha_1 + \alpha_2 - \alpha_3) z_R\end{aligned}$$

Here, z_R denotes the Rayleigh length, Δk the wave vector mismatch[1], ρ the walk-off angle between fundamental and SFG beam, and $\delta_0 = \mathrm{w}_0/z_R$ the beam divergence with the minimum beam radius w_0. One advantage of quasi-phase matching by periodically poled nonlinear crystals is that the angle of incidence can be chosen so that the walk-off angle ρ and with it the double refraction parameter β is zero. According to [36] the absorption is negligible for nominally pure crystals (e.g. $\alpha_3 < 0.01\ \mathrm{cm}^{-1}$). Assuming that the fundamental beams are focused on the crystal center also μ becomes zero and the output power is only dependent on the focusing strength ξ and the phase mismatch σ (Fig. 3.4):

$$h(\sigma, \xi) = \frac{1}{4\xi} \left| \int_{-\xi}^{\xi} d\tau \frac{e^{i\sigma\tau}}{1 + i\tau} \right|^2 \quad . \tag{3.4}$$

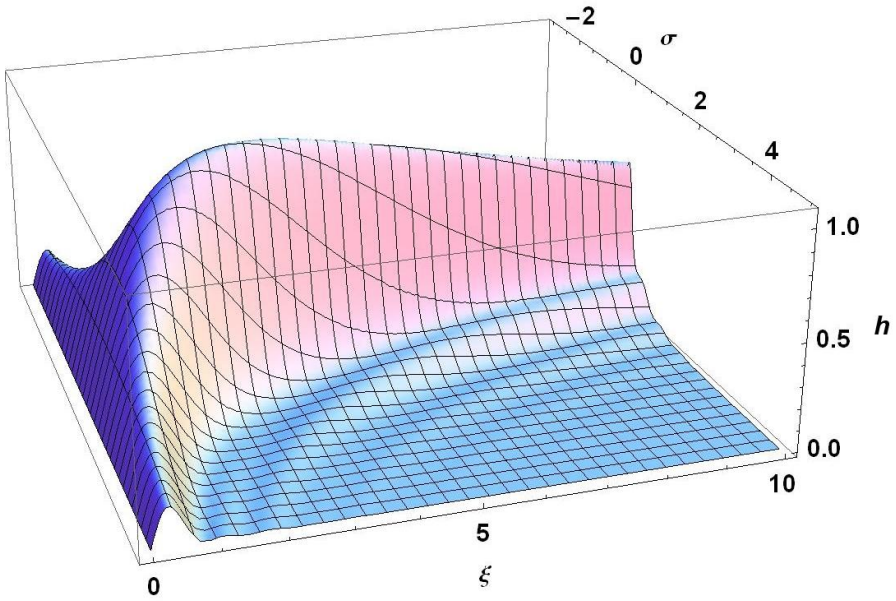

Figure 3.4: 3D-plot of the function $h(\xi, \sigma)$, proportional to the SFG output power, as a function of the phase mismatch σ and the focusing strength ξ. The global maximum of the function, and therewith of the SFG output power, lies at $\sigma = 0.574$ and $\xi = 2.84$.

[1]The wave vector mismatch corresponds to $\Delta k = 2\pi \left[\frac{n_3(\lambda_3,T)}{\lambda_3} - \frac{n_1(\lambda_1,T)}{\lambda_1} - \frac{n_2(\lambda_2,T)}{\lambda_2} - \frac{1}{\Lambda} \right]$ with n_i given by the Sellmeier equation (3.2)

Fig. 3.5 corresponds to a projection of the graph $h(\sigma, \xi)$ in Fig. 3.4 onto the plain of optimum phase mismatch $\sigma_{opt} = 0.574$, to show h as a function of the focusing parameter ξ only. Maximum output power is reached at

$$\xi = 2.84 \tag{3.5}$$

for both fundamentals. This means, our aim is to shape the fundamental beams for the SFG so that their Rayleigh length is

$$z_R = \frac{l}{2 \cdot 2.84} = \frac{20 \text{ mm}}{2.84} = 7.04 \text{ mm}$$

inside the PPLN and that their foci are placed in the center of the crystal. Optimum phase matching is achieved by periodically poling of the $LiNbO_3$ (Sec. 3.1). So, starting from the crystal center, the theoretically optimal q-parameter for both fundamentals is given by

$$q_{center}^{PPLN} = (0 + 0.00704\, i) \text{ m} \quad ,$$

with corresponding beam waists of $58.9\,\mu$m and $47.3\,\mu$m, for 1551 nm and 1000 nm respectively. The propagation through 2 cm of $LiNbO_3$ and the refraction on the planar crystal boundary modifies the q-parameters, depending on the corresponding wavelength and the refractive indices. This evolution is derived via ABCD-matrices (see App. A for the calculation). Therefore, the q-parameters at the outer front surface of the crystal are:

$$\begin{aligned} \text{1550 nm:} \quad & q_{c.border}^{air} = (0.00905 + 0.00319\, i) \text{ m} \\ \text{1000 nm:} \quad & q_{c.border}^{air} = (0.00897 + 0.00316\, i) \text{ m} \end{aligned}$$

This corresponds to beam waists of $39.7\,\mu$m (1551 nm) and $31.8\,\mu$m (1000 nm) in air. With the aid of the Mathematica program in App. B, appropriate optical telescopes were designed, to match to the target q-parameters.

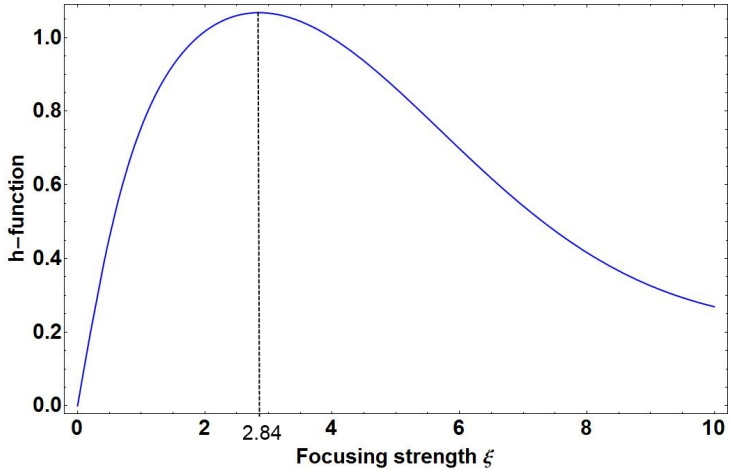

Figure 3.5: Function $h(\xi)$, proportional to the SFG output power, for optimized phase matching $\sigma_{opt} = 0.574$. Absorption, double refraction and focus position are zero. The dashed line marks the value for optimum focusing strength $\xi = 2.84$.

One notices that the optimization is not very sensitive with respect to the focusing parameter: the curve in Fig. 3.5 deviates only 10% from its maximum in the range between $1.6 < \xi < 4.4$.

Therefore, it is relatively straightforward to achieve a high sum-frequency conversion efficiency. With the setup in Sec. 4.2 a focusing strength between $\xi = 1.5 - 3.2$ is obtained.

The focusing strength also affects other characteristics of the SFG process: The graphs in Fig. 3.6 show how the sinc-like pattern, derived in Sec. 2.2.2, changes with respect to the focusing parameter: Compared to the function in Fig. 2.7, an asymmetry shows up, which increases with rising ξ. The contrast of the minima decreases and the spacing of the maxima on the side $\sigma > 0$ enlarges, relative to the side $\sigma < 0$. For very high focusing strengths $\xi \sim 10$ the symmetric interference pattern almost vanishes and only a weak structure of minima is superposed on a gradual decay. This asymmetric development is also visible in the characterization of our generated sum-frequency light (Fig. 4.5).

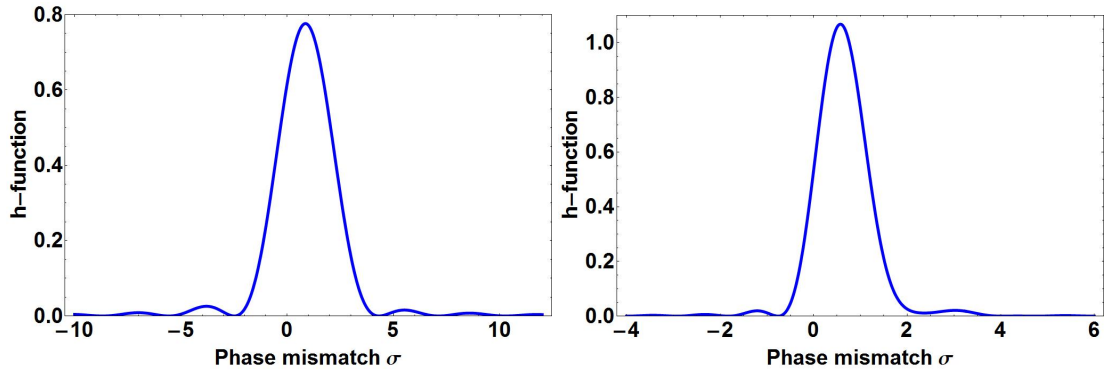

(a) $\xi = 1$ (b) $\xi = 2.84$

(c) $\xi = 5$ (d) $\xi = 20$

Figure 3.6: Function $h(\sigma)$, proportional to the SFG output power, as a function of the phase mismatch σ for selected values of the focusing strength. The phase mismatch is to first order proportional to the crystal temperature. Absorption and double refraction are zero. (a) The familiar, almost symmetric interference pattern is visible (c.f Fig. 2.7). (b) The curve has a similar structure as (a), besides the upcoming asymmetry. (c) The coherence length pattern becomes weaker, the minima in the $\sigma > 0$ region are shifted and the spacing of the minima on the side $\sigma > 0$ is clearly broader than on the side $\sigma < 0$. In (d) the strong focusing pattern is strongly pronounced: a weak structure of equidistant minima is superposed on a gradual decay.

3.3 Ring resonator

The resonant doubling cavities in our SHG devices are designed in a bow-tie ring geometry [37]. They consist of two plane and two concave mirrors, defining the so called “ring resonator”. The nonlinear crystal (LBO or BBO in our case) is located between the two spherical mirrors, at the position of the beam waist. That way, the fundamental laser beam always passes the crystal in the same direction and the resonator acts as build-up cavity, increasing the fundamental laser power at the position of the nonlinear crystal. Thereby the nonlinear effect is enhanced. Fig. 3.7 shows the principle of a ring resonator.

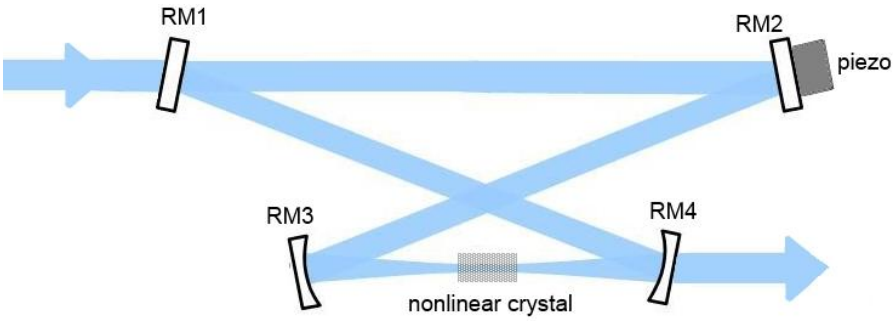

Figure 3.7: Schematic of a resonant doubling cavity designed as a ring resonator. It consists of two plane mirrors (RM1, RM2) and two concave mirrors (RM3, RM4). The nonlinear crystal sits at the beam waist between the concave mirrors. A piezo allows adjusting the cavity length.

The mode behaviour of the cavity is determined by the length of the nonlinear crystal, the mirror spacing, the radii of curvature of the curved mirrors, and the angle of incidence of the light field on the mirrors. Mirror RM1 transmits the fundamental beam partially in a way that the intensity in the ring cavity is maximized. The piezo element on RM2 allows adjusting the cavity length to bring the cavity in resonance to the fundamental laser. Usually, the cavity mirror RM4 is highly transmissive to the converted light so that the cavity is only resonant to the fundamental light. The frequency doubled light beam is extracted through the concave mirror RM4. A photodiode, located behind RM3, allows determining the intra-cavity laser power.

Chapter 4

Laser system for two-photon Rydberg excitation

This chapter contains an experimental analysis of the laser system for the planned excitation of strontium ions from the $4D_{5/2}$ into a Rydberg state above $n = 30$. It includes a description of the optical setup as well as a quantitative characterization of the sum-frequency generation.

4.1 The two excitation steps: $4D_{5/2} \rightarrow 6P_{3/2}$ at 243 nm and $6P_{3/2} \rightarrow n$=30-60 S/D at 305-310 nm

As mentioned in Sec. 2.1, we plan a two-photon excitation to overcome the large energy gap between the $4D_{5/2}$ qubit level and a Rydberg level with a principal quantum number between $n = 30 - 60$.

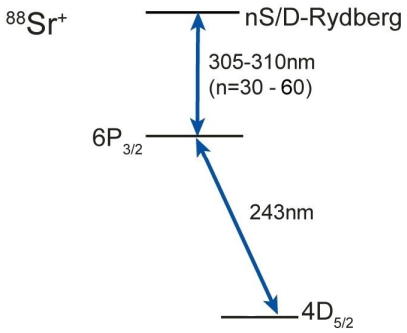

Figure 4.1: Level scheme for the two-photon Rydberg excitation of a $^{88}Sr^{+}$ ion.

The 243 nm light for the **first Rydberg excitation step** is obtained by frequency quadrupling of 972 nm laser light by two cascaded second-harmonic generation processes. Toptica provides a commercial device for this application, the "TA/DL-FHG pro" [37]. A grating stabilized diode laser produces 972 nm light (typically 38 mW), which is amplified in a semiconductor tapered amplifier to typically 620 mW. The second-harmonic light (486 nm) is generated by a LBO crystal, mounted inside a ring resonator[1] to increase the fundamental laser power. The achieved

[1] Sec. 3.3 explains the working principle of the ring resonator.

light (about 210 mW) is again frequency-doubled by a BBO crystal in a second ring cavity, to finally obtain typically 30 mW of 243 nm laser light. The final output power reaches up to 100 mW for higher tapered amplifier currents. The phase matching condition in the crystals is satisfied by angle phase matching. Two optical isolators protect the tapered amplifier and the seed laser diode from back reflections.

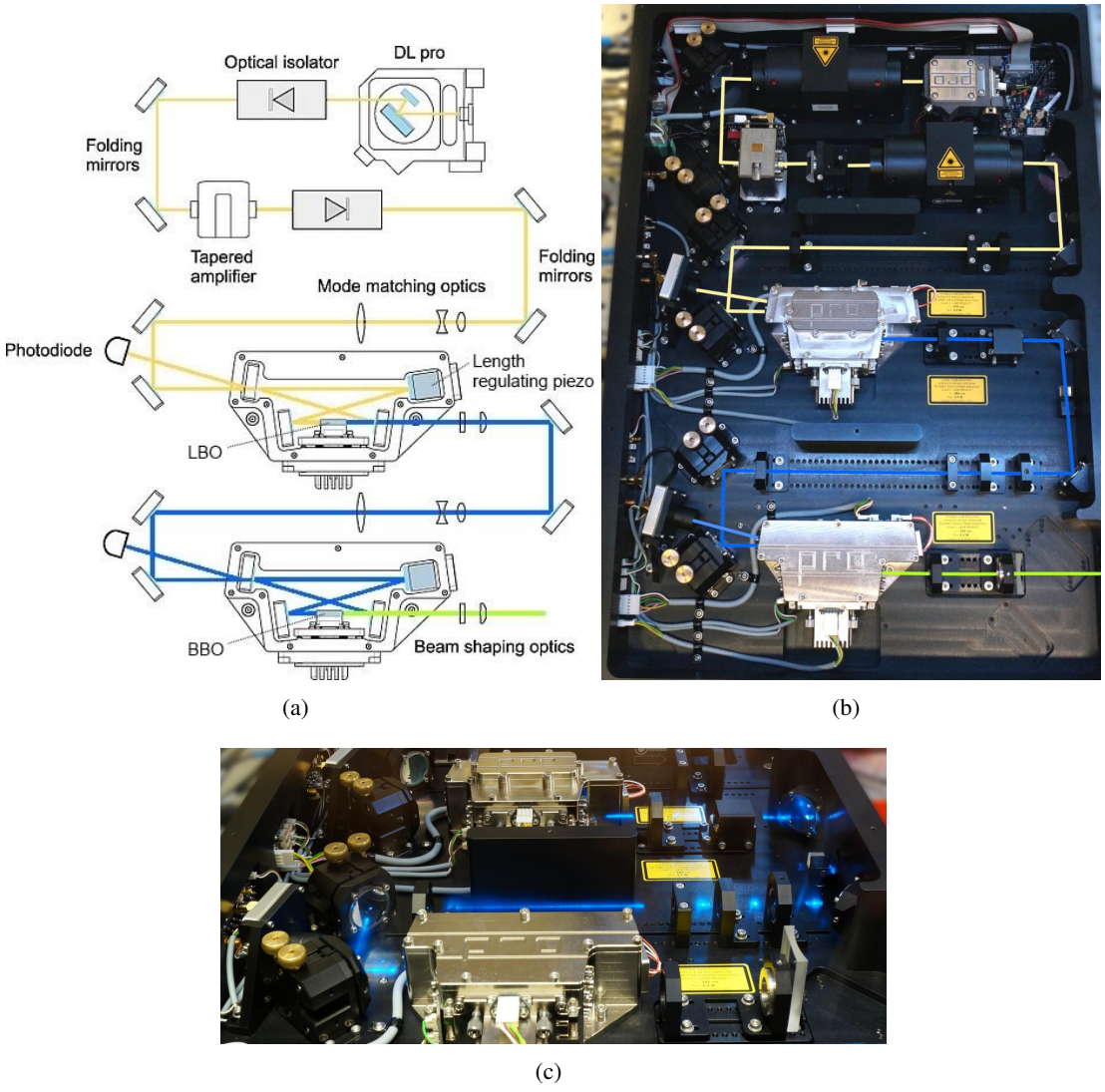

(a) (b)

(c)

Figure 4.2: Setup of the sequenced fourth-harmonic generation device "TA-FHG pro". (a) Schematic setup. The colored lines show the paths of 972 nm (yellow), 486 nm (blue) and the final output light at 243 nm (green). (b) Photograph of the TA-FHG pro. The lines were artificially added to denote the beam path. The line colors and the arrangement of the technical elements correspond to schematic (a). The two SHG-cavities are housed inside the trapezoidal metal cases. (c) Photograph of 486 nm light between the two SHG-cavities. 972 nm and 243 nm are not visible to the naked eye.

The laser light required for the **second excitation step** is more difficult to obtain, since we have special demands: it should have a linewidth $\lesssim$100 kHz and be tunable, to allow excitation to several Rydberg levels above $n = 30$. The following sections describe the laser system to generate laser light at 304-310 nm. The idea is to mix 998-1029 nm and 1551 nm light in a sum-frequency generation process to obtain 607-619 nm, (Sec. 4.2) which is then frequency-doubled to 304-310 nm (Sec. 4.3).

4.2 Sum-frequency generation of 607-619 nm light

The setup for the sum-frequency generation in Fig. 4.3 relies on a similar system for laser cooling and manipulation of Be^+ ions at 313 nm wavelength [16]. In our setup two infrared lasers constitute the fundamental beams for the nonlinear process:

- a tunable 1000 nm diode laser (Toptica) with a build-in tapered amplifier and a maximum output of $\sim$1.5 W and
- a 8 kHz broad, 1551 nm diode laser (TeraXion), which is amplified by a fiber amplifier (Manlight) to a maximum power of 10 W. An additional 5 dB attenuator and two fiber isolators (60 dB and 40 dB isolation) should prevent the master laser from strong back reflections.

The 1551 nm light leaves the amplifier directly through a fiber with an attached collimator, so it has a well defined Gaussian shape. The 1000 nm light leaves the laser box in free space. Since its beam shape is distorted by the tapered amplifier, we couple it into an external fiber as well for mode filtering. Both laser beams pass through polarizing beamsplitter cubes to adopt vertical polarization with respect to the optical table. Their q-parameters are shaped in telescopes in order to satisfy the Boyd and Kleinman condition for optimum frequency conversion efficiency (Sec. 3.2):

$$\xi = \frac{l}{2 \cdot z_R} = 2.84$$
$$\Rightarrow \quad z_R = \frac{40 \text{ mm}}{(2 \cdot 2.84)} = 7.0423 \text{ mm} \ ,$$

for a crystal length of $l = 40$ mm. z_R denotes the theoretically optimal Rayleigh length within the crystal. This corresponds to a beam waist of 47 µm for the 1000 nm beam and 59 µm for the 1551 nm beam. Using ABCD-matrices one derives the corresponding q-parameters (cf. Sec. 3.2) and calculates the corresponding waists in free space: 32 µm and 40 µm respectively. A Mathematica-program (App. B) determines appropriate telescopes for matching the q-parameters: The telescope for the 1000 nm beam consists of a $f_1 = -50$ mm plano-concave and a $f_2 = 100$ mm plano-convex lens. They are spaced by 13.9 ± 0.3 cm and mounted on single axis translation stages for fine adjustment of the spacing and the focus position. The achieved beam waist measures 30 ± 6 µm in free space. The distance between second lens and front surface of the crystal measures 20.5 ± 0.5 cm, so that the waist will be positioned at the center of the crystal. The plano-convex lenses for the 1551 nm beam have focal lengths $f_1 = 100$ mm and $f_2 = 75$ mm. They are spaced by 21.5 ± 0.3 cm and generate a 50 ± 10 µm waist in free space. For a distance of 26.0 ± 0.5 cm between second lens and crystal surface, the beam waist

is sited midway along the crystal's length. The achieved waist sizes are comparable with the theoretical optimal values for both fundamental beams and result in focusing parameters in the range of $1.5 < \xi < 3.2$, close to the optimal value of 2.84.

Next, the two infrared beams are spatially overlapped on a dichroic mirror and the crystal is build in at the distances mentioned above. The crystal itself sits in an oven, mounted onto a translation stage with 5 degrees of freedom. This allows for optimization of the beam propagation through the different periodicity paths. The 1000 nm light path in the crystal is observable with a commercial video camera (after removal of the infrared filter), to ensure that the two fundamentals propagate straight through a selected path. By adjusting the horizontal position of the oven perpendicular to the beam propagation, one can select the path along which the beams propagate through the crystal and thus which poling periodicity they meet. According to Sec. 3.1, the periodicity and temperature of the crystal are chosen such that the phase matching condition is satisfied and maximum output power of 608 nm light is achieved. Finally, the output light field is reflected off three dichroic mirrors in order to filter out the fundamental light components. The remaining 608 nm light is split at a polarizing beam cube to send a small part of the power to a stabilizing cavity and the other part to the SHG device. The generated wavelength can be tuned by adjusting the optical grating of the 1000 nm laser (an external cavity diode laser in Littrow configuration, tunable between 998-1029 nm) as well as the temperature of the PPLN and the respective periodicity path (Sec. 3.1, especially Fig. 3.3). This way it is possible to tune the output light from 607-619 nm.

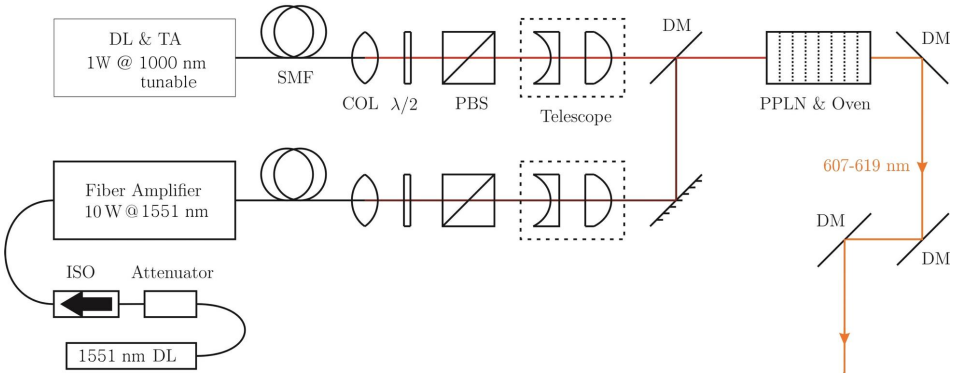

Figure 4.3: Schematic diagram of the optical setup for sum-frequency generation. The infrared light of two diode lasers (tunable 1000 nm and 1551 nm) is summed in frequency in a 4 cm long PPLN to generate 607-619 nm laser light. Dichroic mirrors (DM) are used to overlap the fundamental beams and filter them out of the light field after the sum-frequency process. Polarizing beam splitters (PBS) are used to guarantee that the beams are polarized vertically[2] with respect to the optical table and together with the half-wave plates ($\lambda/2$) they can be used to fine-adjust the optical power of the fundamental beams. The telescopes shape the Gaussian beams so that they satisfy the condition for optimum frequency conversion (Boyd and Kleinman, Eq. (3.5)). ISO: optical isolator, DL: diode laser, TA: tapered amplifier, SMF: single-mode fiber, COL: collimator, PPLN: periodically poled lithium niobate crystal.

[2]The polarization of the fundamental beams must be aligned with the dipole moment of the crystal to utilize the nonlinear properties of the PPLN. Light polarized horizontally with respect to the optical table will be transmitted through the crystal unaffected.

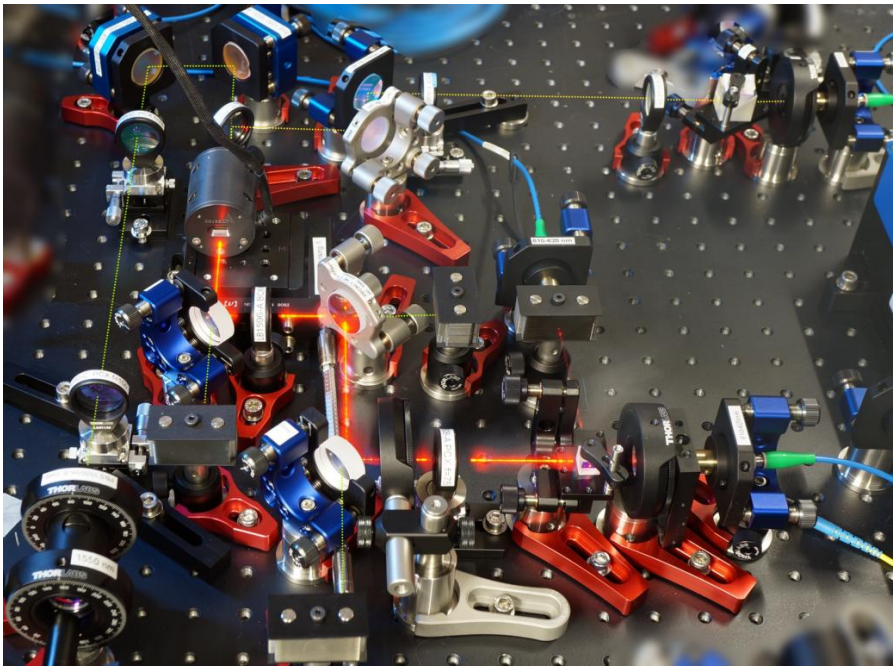

Figure 4.4: Photograph of the SFG Setup. Starting from the collimator the entire paths of the infrared fundamental beams can be followed. The 1551 nm light starts from the lower left corner and is artificially indicated by a thin, dashed green line. The 1000 nm beam begins in the upper right corner and is indicated by a thin, dashed yellow line. The cylindrical black object close to the upper left corner is the crystal oven, the origin of the visible orange 608 nm laser beam. Three black beam blocks are mounted directly behind the dichroic mirrors, which transmit the remaining fundamental components for filtering. The two blue fibers send the 608 nm light to a stabilizing cavity and the SHG setup respectively.

4.2.1 Characterization

In order to characterize the 607-619 nm light, the 1000 nm laser is first tuned to 1010 nm and the middle path of the PPLN, with a periodicity of 10.70 µm, is chosen. A crystal temperature around 130 °C is required (cf. Sec. 3.1) to satisfy the phase matching condition. Thereby, laser light at a wavelength of 612 nm is generated by mixing 1010 nm and 1551 nm fundamental beams in the PPLN crystal.

As calculated in Sec. 2.2.2 the output power has a sinc-like dependency on the phase mismatch. Since the temperature of the crystal is (to first order) proportional to the phase mismatch, the output signal plotted against the temperature will also show a sinc behaviour. Regarding Boyd and Kleinman [35], this function can show asymmetries in the case of strong focusing (cf. Fig. 3.6 (c)), which goes hand in hand with the condition of optimal conversion in Eq. (3.5). This asymmetry is visible in Fig. 4.5, where the 612 nm power is plotted as a function of the crystal temperature. The error bars account for power fluctuations and uncertainties in the temperature measurement.

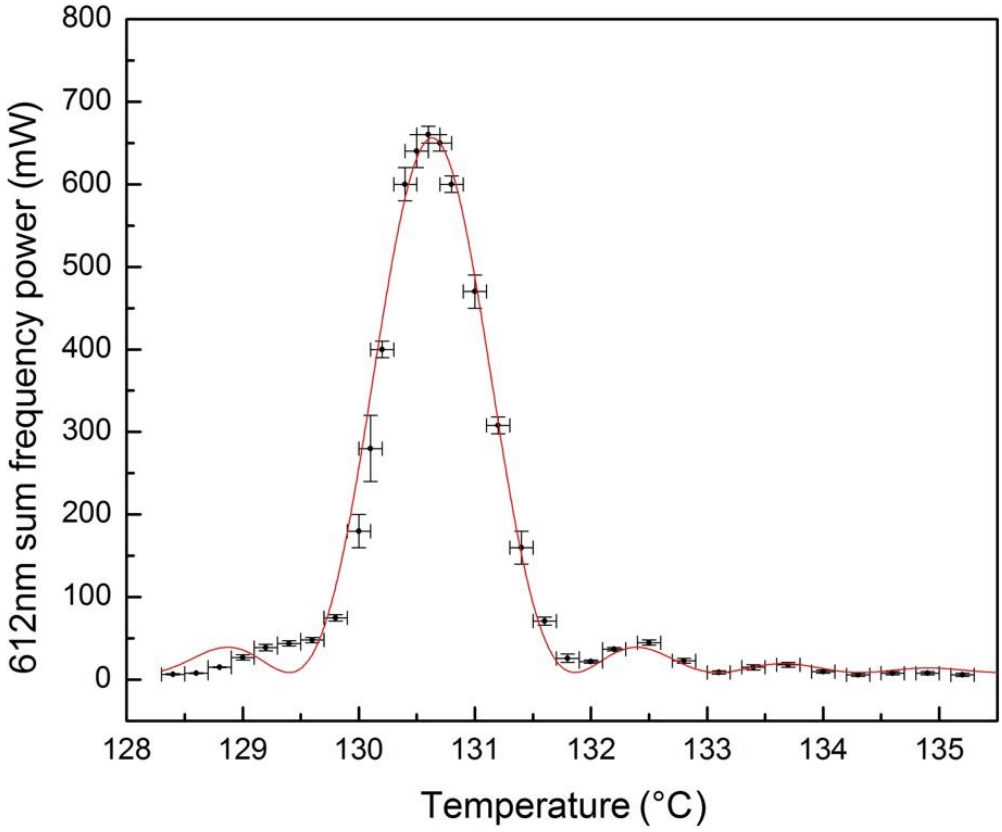

Figure 4.5: SFG output power as a function of the PPLN temperature. The red curve is a modified (shifted and scaled) sinc-plot, which shows that the measurement is consistent with the calculated behaviour in Fig. 2.7. The asymmetry at lower temperatures is due to strong focusing, which is linked to the condition of optimum conversion efficiency [35]. The maximum output power of 650 mW (for 1010 nm and 1551 nm pump lasers) is achieved at a temperature of 130.6 °C, the FWHM measures 1.1 °C.

One notices that the output power reaches it's maximum at 130.6 °C, which does not exactly correspond to the expectations in 3.1. This means that the specified, theoretical Sellmeier curves (Fig. 3.3) deviate slightly from the experimental data for this crystal. We further investigate this effect by experimentally reconstructing the Sellmeier curves: The temperature maximum is measured for different detuning of the 1000 nm laser and for several poling periodicities, over the entire wavelength range of interest[3]. Fig. 4.6 shows the result. The error bars include uncertainties in temperature measurement and wavelength reading of the wavelength meter (HighFinesse). For the $10.40\,\mu$m Sellmeier line only two data points are measured because the lower tuning threshold of the 1000 nm laser is reached. Therefore this Sellmeier line is not very precise. Fig. 4.7 reveals the difference between the theoretical (gray) Sellmeier curves, derived in Sec. 3.1 and the experimental (colored) Sellmeier curves.

[3]Tunability of the 1000 nm laser between 998-1029 nm is necessary in order to generate laser light of 304-310 nm and enable excitation into Rydberg states between $n = 30 - 60$ (cf. Fig. 3.3).

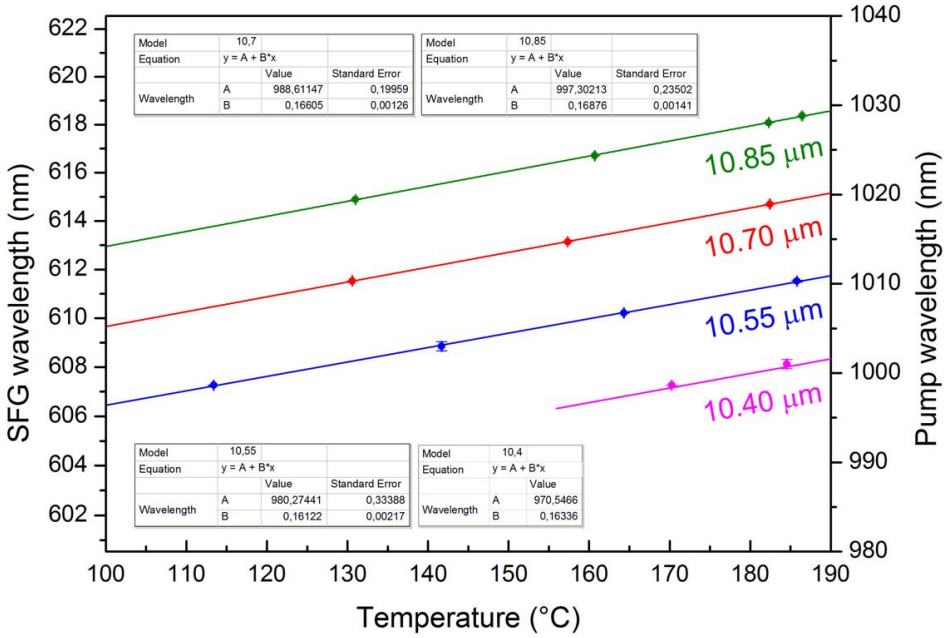

Figure 4.6: Measured Sellmeier curves over the area of interest. The graph shows the tunability of 607-619 nm output light. The first pump laser is fixed at 1551 nm while the second pump laser is tuned between 998-1029 nm. The theoretical curves were approximated with lines, with different colors denoting different crystal periodicities, specified by the attendant colored numbers.

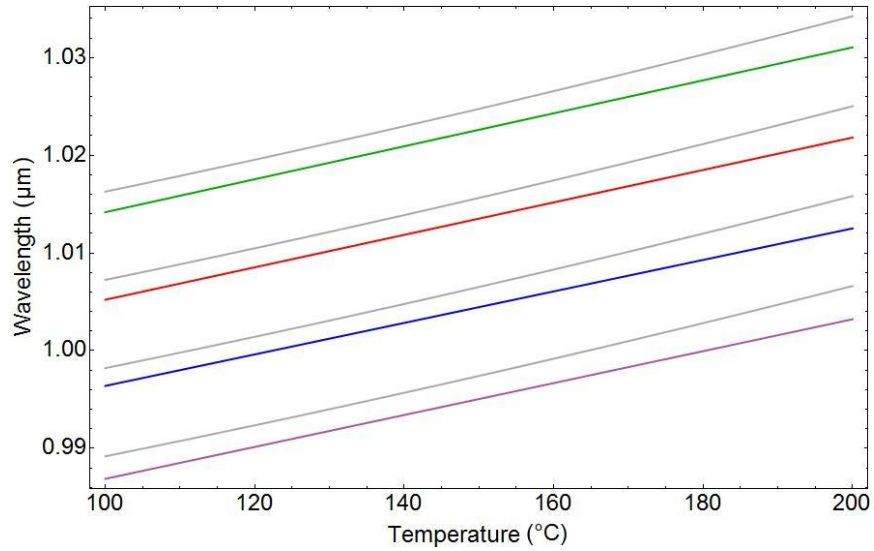

Figure 4.7: Comparison of the measured (colored) with the theoretically calculated Sellmeier curves (gray). The colors of the lines denote the crystal periodicities: 10.85 µm (green), 10.70 µm (red), 10.55 µm (blue), 10.40 µm (purple). The slopes of the curves are comparable but the differing offsets seem to indicate that the specified poling periodicities are wrong.

To first order, the experimentally determined lines are shifted towards lower wavelengths relative to the theoretical curves. Equation (3.1) indicates that such an offset could be explained by slightly different poling periodicities, which would mean that the specified crystal periodicities are inaccurate. In order to find the matching poling periodicity values, the four theoretical curves are adapted until they roughly overlap with the experimental lines (Fig. 4.8). Table 4.1 shows a first correction of the crystal periodicities.

$10.85\,\mu m$	$\rightarrow$	$10.823\,\mu m$
$10.70\,\mu m$	$\rightarrow$	$10.674\,\mu m$
$10.55\,\mu m$	$\rightarrow$	$10.527\,\mu m$
$10.40\,\mu m$	$\rightarrow$	$10.369\,\mu m$

Table 4.1: First correction of the crystal periodicities. The specified values on the left are replaced by the empirically determined values on the right.

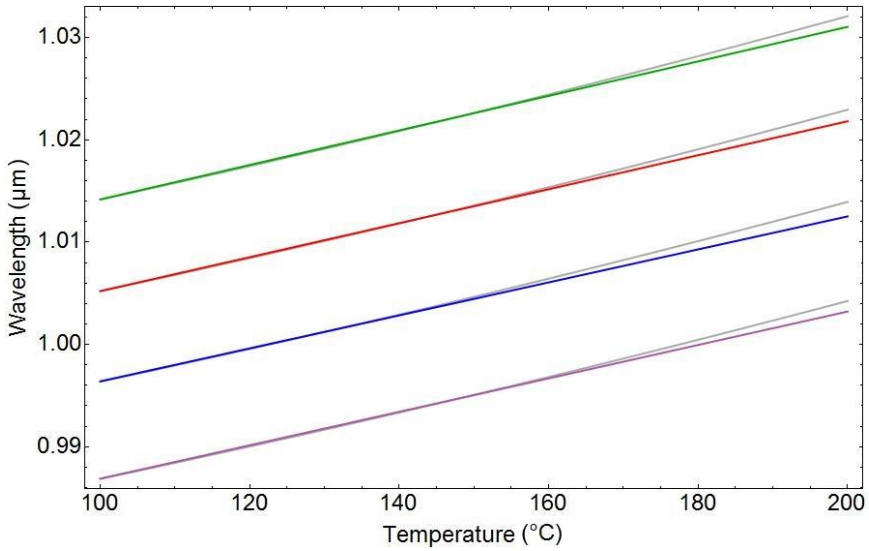

Figure 4.8: Theoretical Sellmeier curves (gray) adapted to the experimentally measured lines (colored). The line colors denote the different modified crystal periodicities: $10.823\,\mu m$ (green), $10.674\,\mu m$ (red), $10.527\,\mu m$ (blue), $10.369\,\mu m$ (purple). The correction matches for the most part of each curve. At higher temperatures the experimental lines do not follow the bending of the theoretical curve. Further analysis shows that it is not the approximation of a linear relationship which causes the deviation.

After correcting the periodicities of the theoretical curves, they still deviate from the experimentally obtained lines at higher temperatures. One could assume that it is caused by fitting the data with only a straight line, however, the theoretically predicted curve does not match the measured data points in this region, even considering error bars. Fig. 4.9(a) illustrates this for the case of the Sellmeier line with the largest error bars. According to Eq. (3.2), b_1 is one parameter which is responsible for the slope of the Sellmeier curves. According to [31], it accounts for thermal effects in the crystal. The other parameters which could compensate for the deviation

are strongly correlated. Moreover, the characteristics for which they account in the equation are more difficult to estimate. Therefore, the b_1 parameter is adjusted in order to correct for the slope difference. Additionally, the periodicities are corrected once more until the theoretical curve touches the three data points, within the error bars (see Fig. 4.9(b)).

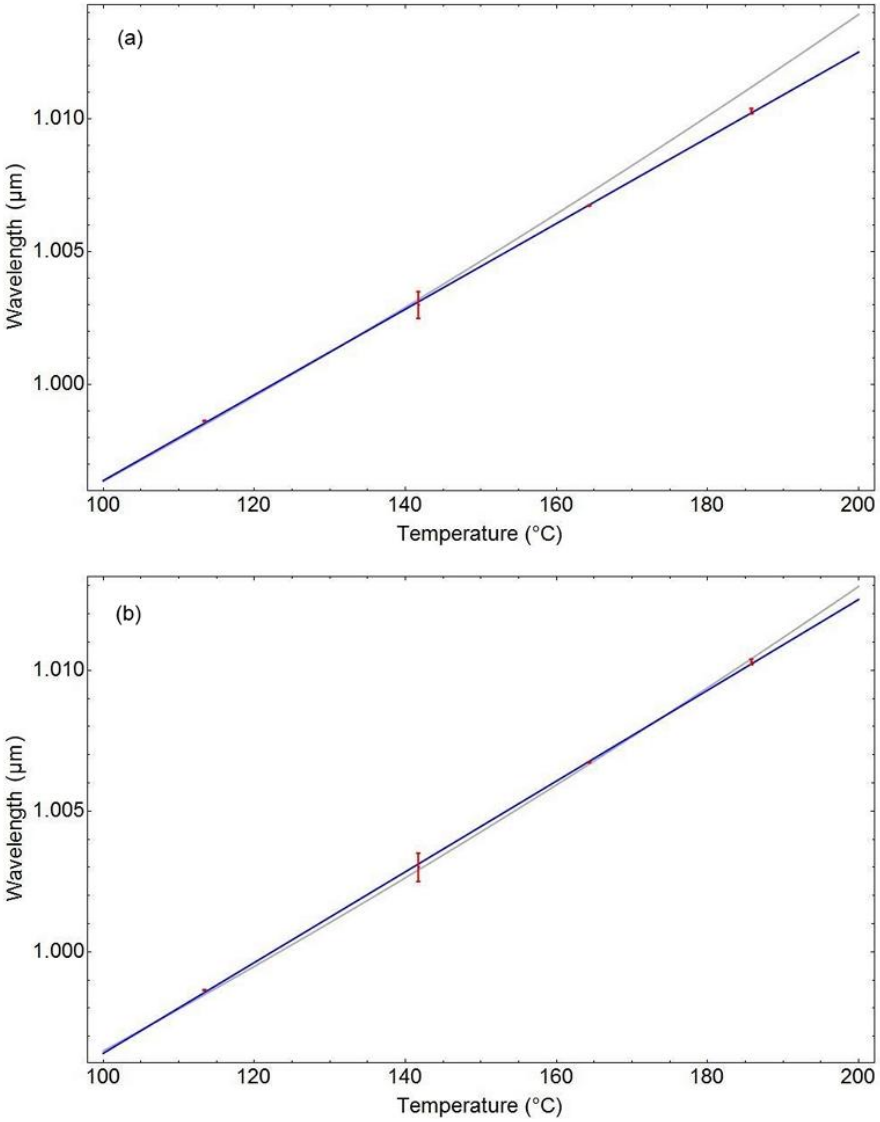

Figure 4.9: Comparison between theoretically predicted Sellmeier curve and measurement, on the example of the $10.527\,\mu m$ periodicity. The theoretical curve is gray, the red dots and error bars are measurement data and the blue line is a linear fit of the measurement points. Graph (a) shows the status after the first periodicity adaptation ($10.55\,\mu m \rightarrow 10.527\,\mu m$). A strong slope deviation at the high temperature region remains so that the theoretical curve does not cover all data points, even considering error bars. In graph (b) the b_1-parameter is modified ($2.860 \cdot 10^{-6} \rightarrow 3.060 \cdot 10^{-6}$) and the periodicity is once more adapted ($\rightarrow 10.540\,\mu m$), to achieve a sufficient overlap between theory and measurement.

The modifications of the b_1 parameter and of the crystal periodicities are finally applied onto all five periodicity paths. The result is visible in Fig. 4.10 and summarized in table 4.2. The deviations from the specified periodicities lie around 10 nm. The biggest deviation (14 nm) is registered at the $10.40\,\mu m$ periodicity, which was only fitted by two measurement points and is therefore not very reliable. The obtained graph is used to tune the wavelength generated by the sum-frequency process fast and efficiently between 607-619 nm.

b_1: $2.860 \cdot 10^{-6}$	$\rightarrow$	$3.060 \cdot 10^{-6}$
$10.823\,\mu m$	$\rightarrow$	$10.841\,\mu m$
$10.674\,\mu m$	$\rightarrow$	$10.689\,\mu m$
$10.527\,\mu m$	$\rightarrow$	$10.540\,\mu m$
$10.369\,\mu m$	$\rightarrow$	$10.386\,\mu m$

Table 4.2: Final correction of the b_1 parameter and the crystal periodicities. The specified values on the left are replaced by the empirically determined values on the right.

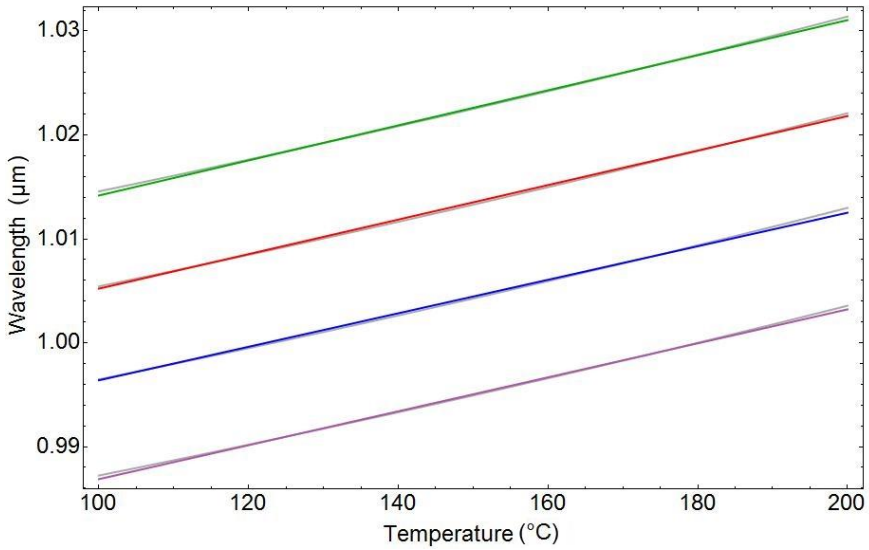

Figure 4.10: Final adapted Sellmeier curves in the region of interest. The b_1-parameter and the specified crystal periodicities are corrected until sufficient overlap between theoretical specified curves (gray) and experimentally determined lines (colored) is reached. The colors denote the different modified crystal periodicities: $10.841\,\mu m$ (green), $10.689\,\mu m$ (red), $10.540\,\mu m$ (blue), $10.386\,\mu m$ (purple).

With these results we can theoretically simulate the behaviour of the SFG output power as a function of the temperature (representing the phase mismatch[4]) according to the plots in Fig. 3.6. Double refraction and absorption can be considered to be zero and the foci of our

[4]The temperature is in first order proportional to the phase mismatch $\sigma = z_R \cdot \Delta k = z_R \cdot 2\pi \left[\frac{n_e(\lambda_3,T)}{\lambda_3} - \frac{n_e(\lambda_1,T)}{\lambda_1} - \frac{n_e(\lambda_2,T)}{\lambda_2} - \frac{1}{\Lambda}\right]$, with n_e given by the Sellmeier equation (3.2).

fundamental beams are positioned in the center of the crystal so that we can use the function h from Eq. (3.4) to simulate the behaviour of the SFG output power. Fig. 4.11(a) shows the theoretical simulation for $\lambda_1 = 1010$ nm, $\lambda_2 = 1550.9$ nm, $\Lambda = 10.6894$, and $\xi = 3.2$. It is in good agreement with the experimental result, reproduced in Fig. 4.11(b). The deviation in shape at lower temperatures may be caused by an inhomogeneous temperature profile within the crystal, resulting in an effective gradient in the refractive index. Possible causes for this effect are inhomogeneous heating of the crystal by the oven or thermal lensing[5].

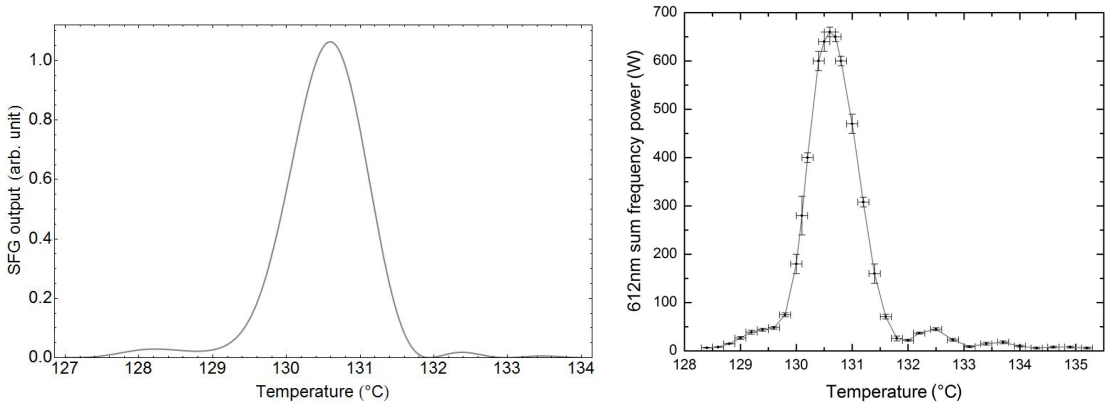

(a) (b)

Figure 4.11: Theoretically simulated (a) and experimentally determined (b) SFG output as a function of the crystal temperature. The maximum lies around 130.6 °C and the asymmetry, caused by strong focusing, is visible in both graphs. The deviation in shape at lower temperatures could be caused by a temperature-gradient in the crystal. The sinc-like pattern on the right-hand side of the maximum is apparent in both graphs.

Next, the conversion efficiency η of the SFG is analyzed.

$$\eta = \frac{P_{612}}{P_{1010}P_{1551}} \cdot \frac{1}{l} \quad , \tag{4.1}$$

where $P_{612/1010/1551}$ refers to the power of the beam with wavelength 612 nm,1010 nm or 1551 nm and $l = 4$ cm denotes the length of the crystal. The first part of Eq. (4.1) is determined by measuring the output power of 612 nm versus the product of input powers of the two fundamental lasers. Fig. 4.12 shows this measurement. It contains two series: First the 1551 nm power is fixed at 8.68 $\pm$ 0.06 W and 1010 nm is varied between 264-837 mW and secondly the 1010 nm power is fixed at 800 $\pm$ 20 mW and 1551 nm is varied between 2.39-9.07 W. The maximum obtained output power at 612 nm is 650 mW. The individual data points correspond to efficiencies between 2.1-2.5%. The slope of a line fit through all data points leads to an overall efficiency of

$$\eta = \frac{(0.093 \pm 0.004)\ \%}{4\ \text{cm} \cdot \text{W}} = (2.3 \pm 0.1)\%\ \text{W}^{-1}\text{cm}^{-1} \quad .$$

[5]The absorption of laser light is enhanced at the beam focus so that the crystal heats up in the region of the beam focus.

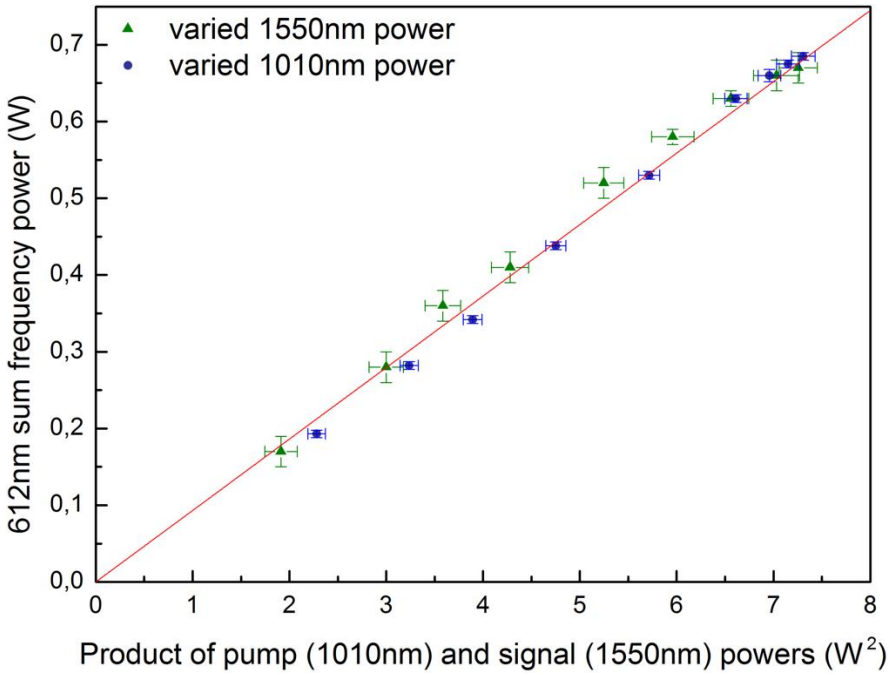

Figure 4.12: SFG output power versus the the product of the input powers. The blue dots are measurement data where the power of the 1551 nm laser is fixed at ∼8.7 W and the power of the 1010 nm laser is tuned. The green dots denote data where 1010 nm is fixed at ∼800 mW and the 1551 nm power is varied. The error bars arise from uncertainties in the power measurements. The red curve is a line plot where both series of measurement were taken into account equally.

4.3 Frequency doubling to 304-310 nm

Similar as the FHG device, the setup for the frequency doubling of the 607-619 nm light into 304-310 nm is a commercial system, provided by Toptica. The "SHG pro" uses an LBO crystal, mounted inside a ring resonator (Fig. 4.13(a)). An universal fiber coupler couples the 607-619 nm light into the device. The beam is shaped by mode matching optics and sent into the resonant doubling cavity by two folding mirrors. Also the 304-310 nm beam is shaped into a collimated, symmetric beam, before it leaves the device. Similar to the "TA/DL-FHG pro" the phase matching condition is satisfied by angle phase matching. So, once the wavelength of the fundamental beam is tuned, the angle of incidence has to be modified to satisfy momentum conservation. For that purpose the nonlinear crystal is mounted on a horizontally shiftable and tilting stage. Additionally, the outcoupling mirror RM4 (and eventually mirror RM3) has to be readjusted in such a way that the beam propagates straight through the final beam shaping optics and the output slit. The position of one of the mirrors is controlled with a piezo, thereby allowing stabilization of the doubling cavity length to be resonant to the wavelength of the 607-619 nm light (subsection 4.4).

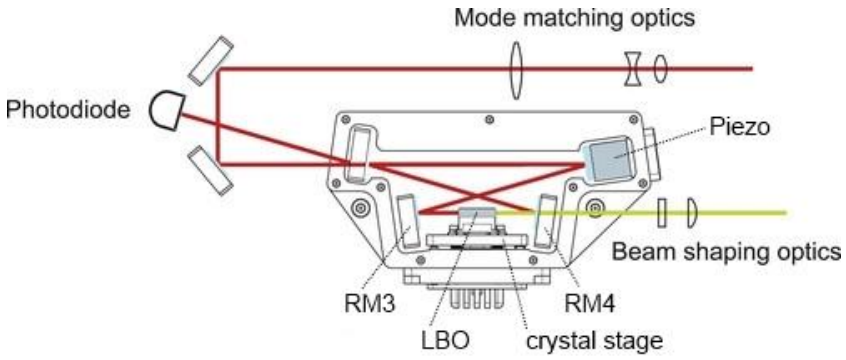

(a)

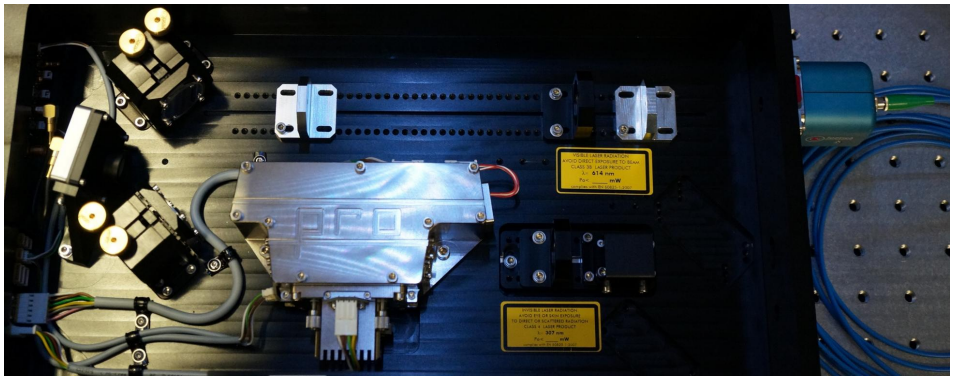

(b)

Figure 4.13: Setup of the second-harmonic generation device "SHG pro". (a) Schematic setup. The red line shows the path of the 607-619 nm light, the green line denotes the UV light (304-310 nm), generated by the LBO crystal. (b) Photograph of the SHG pro. The SHG cavity is arranged inside the trapeziodal metal case. The position of the individual optical elements corresponds to the arrangement in picture (a).

Sending 100 mW of 612 nm into the SHG device and stabilizing the doubling cavity to the input light, a conversion efficiency of $(6.0 \pm 0.5)\%$ is measured. Note that during this measurement the 612 nm linewidth was not narrow because of high-frequency noise on the 1551 nm master laser. Once this problem is solved, a conversion efficiency of up to 30% is expected, as this was observed during installation, where 260 mW of 612 nm fundamental laser light were converted to 75 mW of 306 nm laser light. Therefore, the desired power of 5 mW at 306 nm (derived in Sec. 2.1.2) is feasible.

4.4 Stabilization of the 304-310 laser light

As estimated in subsection 2.1.2 a laser linewidth of $\Delta\nu \lesssim 100$ kHz is required for the Rydberg excitation lasers. A narrow linewidth of the 304-310 nm laser requires frequency-stable fundamental lasers. The linewidth of the 1551 nm master laser is specified to be on the order of 10 kHz, whereas the tunable 1000 nm laser has to be stabilized to an external cavity, with a linewidth of $\Delta\nu^{cav} = 214$ kHz and a finesse around $\mathcal{F} \approx 7000$. We built this cavity in-house,

according to a design of Muir Kumph[6]. It is a four-rod cavity, consisting of four different cavities, mounted on a single ultra low expansion (ULE) glass cylinder inside a vacuum chamber. Fig. 4.14 shows a sketch of the mount for the concave cavity mirrors, where two piezo rings are mounted in such a way that they will expand/contract in opposite directions. Therefore, temperature fluctuations are partially compensated and affect the cavity length to a lesser extent. Some building steps and the complete cavity system are visible in Fig. 4.15.

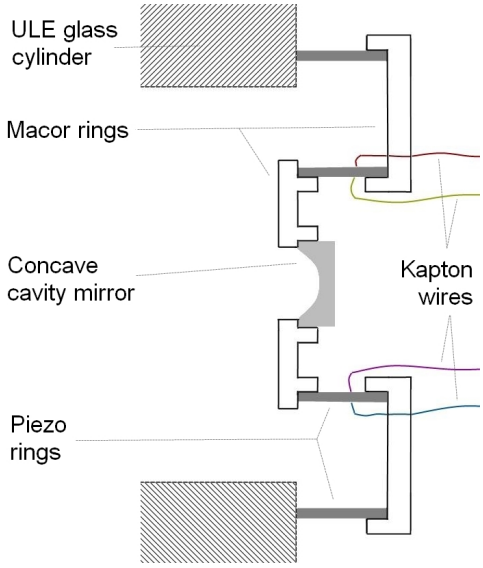

Figure 4.14: Mounting stage for the concave cavity mirrors in cross section. Two Macor ceramic rings connect the piezo rings, which can be driven by the colored, vacuum compatible Kapton wires (c.f. Fig. 4.15(a)). The outer piezo ring is fixed onto the ULE glass cylinder, which provides a stable spacing between the two cavity mirrors (c.f. Fig. 4.15(b),(c)). With this setup temperature fluctuations affect the cavity length to a lesser extent because the two piezo rings mutually compensate for their temperature dilatation.

The frequency stabilization of a laser to the respective cavity is performed through the Pound-Drever-Hall (PDH) method [38, 39]. This technique stabilizes the laser frequency by actively tuning the laser so that it is resonant to a stable reference cavity. In our case, the stabilization loop starts at the Digilock 110 module[7] which modulates the laser current (phase modulation) at 20 MHz frequency, resulting in sidebands of opposite phase around the carrier frequency in the laser frequency spectrum. This modulated light field is sent towards a stable two-mirror cavity in which the carrier signal gains a phase shift, causing an intensity modulation in the cavity-reflected signal. The strength and the direction of the frequency mismatch between the laser and the reference frequency set by the cavity, are stored in this intensity modulation. A photodiode converts the cavity-reflected light field into an electronic signal which is then demodulated to selectively filter the frequency mismatch information (the so called “PDH error signal”). A PID regulator circuit converts the PDH error signal into a correction signal for the laser frequency stabilization.

[6] At this time M.Sc. at the Institute of Experimental Physics, University of Innsbruck. *Muir.Kumph@uibk.ac.at*

[7] The Digilock 110 is a digital laser stabilization module from Toptica. It contains the electronics to generate error signal and feedback current/voltage to control laser frequency fluctuations, according to the PDH method.

In our system, the demodulation happens in the Digilock module itself. We feed in the reflection signal of the cavity and receive the error signal for the PDH-based frequency stabilization. The electronic control unit in the Digilock also contains two adjustable Proportional-, Integral-, and Derivative regulators to stabilize the laser frequency: one optimizes the feedback voltage to the optical grating in the diode laser and the other optimizes the current-correction signal going to the laser diode. After the stabilization of the 1000 nm laser we estimate a satisfying linewidth of $\Delta\nu^{1000} \sim 30$ kHz. Similar to the 1000 nm stabilization cavity, external cavities were built for the 607-619 nm and 1551 nm light to check their linewidths. The 607-619 nm cavity may optionally be used to stabilize the 607-619 nm light by regulating the 1000 nm laser.

The next step towards a narrow linewidth for the 304-310 nm light is to lock the SHG cavity [37] to the 607-619 nm light in order to increase the intensity of the circulating wave and thereby enhancing the nonlinear effect. One of the ring resonator mirrors is mounted on a piezo to adjust the cavity length (Sec. 3.3) and the corrective signal is generated by a commercial, PDH based PID module (Toptica: PID 110). This module employs the sidebands, which were originally modulated on the 1000 nm laser but are still visible after the sum-frequency generation.

From the transmitted signal of the SHG cavity we estimate a lower limit for the 607-619 nm linewidth of $\Delta\nu^{612} \gtrsim 1$ MHz, which corresponds to $\Delta\nu^{306} \gtrsim 2$ MHz for the 304-310 nm light. This is much broader than the target value of 100 kHz. After checking all possible problem sources we come to the conclusion that the 1551 nm master laser has a much broader linewidth than expected. Even the stabilization of the 1000 nm light (when stabilizing 612 nm to the cavity) can not compensate for this high-frequency noise. An additional fiber isolator of 60 dB, between the amplifier and the 1551 nm master laser, did not solve the problem so the spectral properties of this laser need further investigation to allow generation of 304-310 nm laser light with a linewidth below 100 kHz.

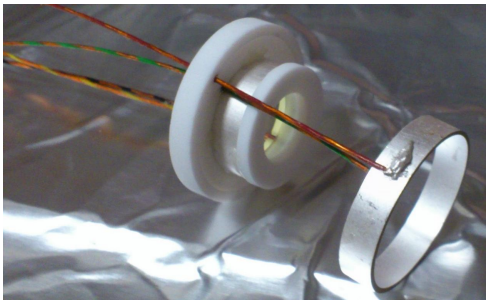

(a)

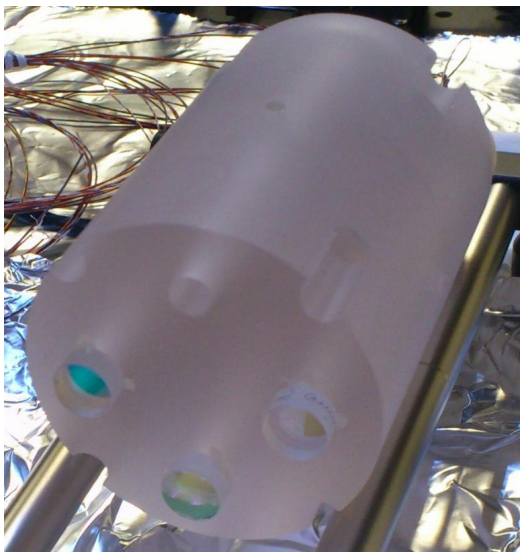

(b)

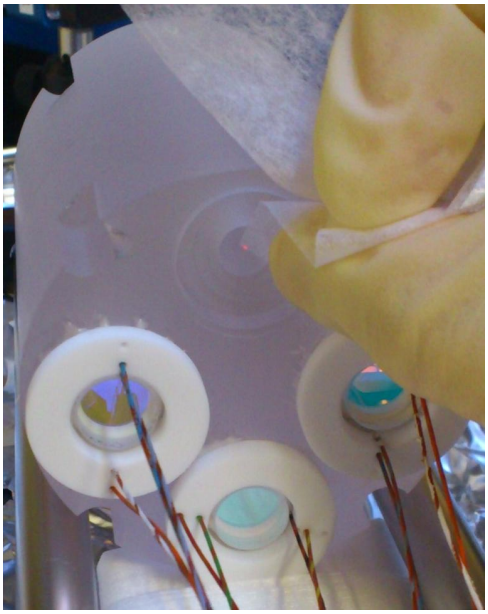

(c)

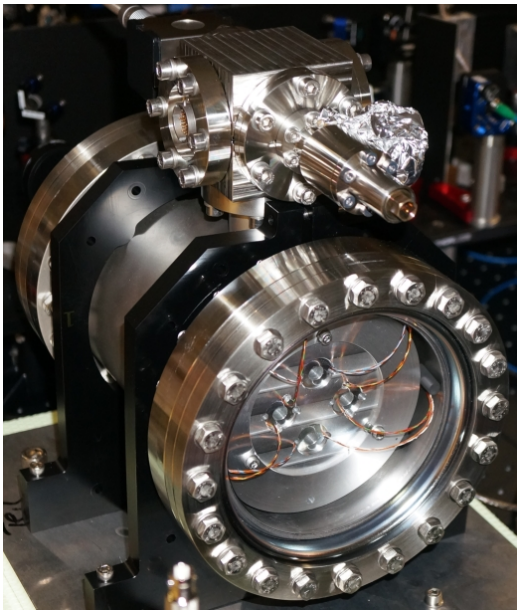

(d)

Figure 4.15: Photographs of some building steps and the complete four-rod cavity for frequency stabilization of four lasers. Picture (a) shows a concave mirror and piezo rings mounted on Macor rings (Fig. 4.14), one step before gluing the outer piezo onto the larger Macor ring. The cavity mirror (yellowish element in the center), the colored Kapton wires and the inner piezo ring are already assembled. Here, the Macor rings, the mirror, and the piezos are connected through UV curable glue, whereas the wires are bonded to the piezos via electrically conductive silver-epoxy. (b) and (c) illustrate how the planar cavity mirrors and the mounted concave mirrors of (a) are glued onto the cylindrical ULE glass spacer. In picture (d) the cavity system is placed into a cylindrical vacuum chamber. The Kapton wires, behind the viewport, are connected to the vacuum feedthrough at the left side of the upper cube. The adapter on the front is the valve for connecting a turbo-molecular pump. The ion getter pump, connected to the back side of the cube, is barely visible.

Chapter 5

Summary and Outlook

The aim of this master thesis was to set up and characterize a laser system for exciting strontium ions into Rydberg states. The planned two-photon excitation scheme requires two UV lasers of 243 nm and 305-310 nm.

We first estimated the required specifications of these lasers: The tunability of the 305-310 nm laser light should allow exciting the ions into any Rydberg state between $n = 30 - 60$. Based on discussions on the wave functions of the involved transitions, we estimated that we can achieve an effective two-photon Rabi frequency between 2π 1.5 MHz $< \Omega < 2\pi$ 13 MHz with a power of 5 mW and a beam waist of 5 µm. Therefore, excitation and de-excitation can succeed before the spontaneous decay of the Rydberg state since the estimated Rabi frequency is much higher than the typical linewidth of the addressed Rydberg level (kHz-regime). Moreover, we want the linewidths of the Rydberg excitation lasers to be below 100 kHz (much smaller than the effective Rabi frequency) so that the phases of excitation and de-excitation coincide.

The 243 nm laser light for the first Rydberg excitation step is commercially available. It is generated by two cascaded second-harmonic generation processes of 972 nm laser light. The typical output power of 30 mW at 243 nm meets the desired specifications for generating a Rabi frequency of several megahertz.

The generation of the 305-310 nm laser light for the second excitation step is performed by sum-frequency mixing of 1551 nm and tunable 1000 nm laser light in a MgO-doped PPLN crystal and subsequent second-harmonic generation in a commercial system. Setting up and characterizing this system was the main topic of this master thesis. The SFG output power shows a sinc-like dependence on the phase mismatch (temperature tuning) superposed by a slight asymmetry, which is consistent with the discussed theory [35]. The SFG efficiency was measured to be $\eta = (2.3 \pm 0.1)\%$ W^{-1}cm^{-1} at 612 nm, employing the 10.7 µm periodicity path at a crystal temperature of 130.6 °C. Mixing 840 mW of 1010 nm and 8.68 W of 1551 nm in the PPLN crystal we achieved a maximum output power of 650 mW at 612 nm. Unfortunately, the frequency of the excitation lasers could not yet be stabilized to linewidths below 100 kHz because one of the fundamental lasers still shows high-frequency noise and needs further investigation. Moreover, we tested and adapted the Sellmeier curves for the five gratings of different periodical poling in our PPLN crystal in order to allow fast and efficient tuning of the SFG wavelength. We could show that the SFG output wavelength is tunable between 607-619 nm, which transforms to 304-309 nm after frequency-doubling. Together with the commercial 243 nm laser this wavelengths allow excitations into any Rydberg state above $n = 30$ (up to double ionization).

At the moment of writing, the ion trap for the strontium ions is being set up[1] and in the near future the laser system of this thesis will be tested for Rydberg excitation. The Rydberg excitation might not be very efficient at the beginning, therefore, a reliable and sensitive method to prove a successful Rydberg excitation is required. One possible, very sensitive method would be fluorescence detection via so called "electron shelving" (Fig. 5.1).

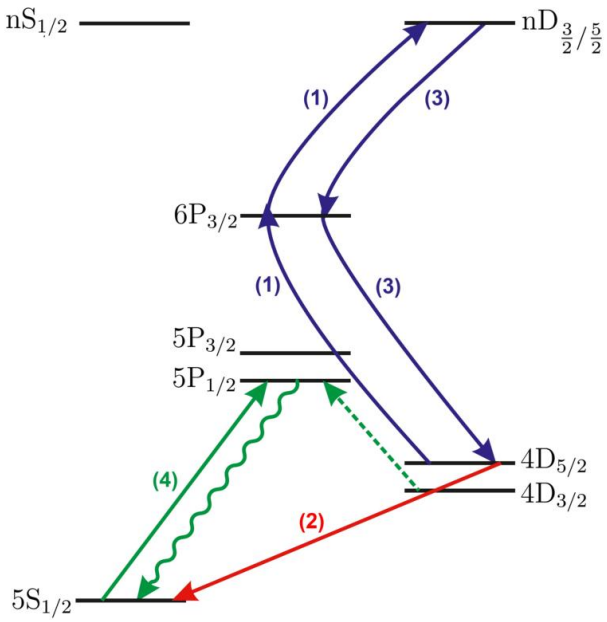

Figure 5.1: Electron shelving scheme for detecting successful Rydberg excitation. The detection scheme consist of five steps: (0) Initial state preparation $4D_{5/2}$, (1) Rydberg excitation, (2) Hiding in the $5S_{1/2}$ state, (3) De-excitation from the Rydberg state, (4) Fluorescence detection: dark (no fluorescence) signals successful Rydberg excitation, bright (fluorescence) signals that the $5S_{1/2}$ state was populated and no Rydberg excitation was achieved.

The electron shelving detection scheme consist of five steps:

0. Prepare the ion in the $4D_{5/2}$ state
1. Excite the ion into the Rydberg state (two-photon excitation)
2. Hide the remaining population in the $5S_{1/2}$ state
3. De-excite the ion from the Rydberg state to the initial $4D_{5/2}$ state
4. Fluorescence detection: $5S_{1/2} \rightarrow$ bright, $4D_{5/2} \rightarrow$ dark. Detection of emitted 422 nm light indicates that the Rydberg state was not excited, while no fluorescence indicates that Rydberg excitation was successful.

[1]The detailed scheme of our linear Paul trap with corresponding direction of optical access and focusing techniques are summarized in the master thesis of Fabian Pokorny - at this time B.Sc. at the Institute of Experimental Physics, University of Innsbruck.

An alternative possibility would be to excite the ion into the Rydberg state and wait until it decays, so that population is found (with a high probability) in the $5S_{1/2}$ state. Whether or not the Rydberg excitation was successful will be tested by observing the fluorescence rate on the $5S_{1/2} \leftrightarrow 5P_{1/2}$ transition, while scanning the second Rydberg excitation laser: On resonance with a Rydberg state the fluorescence rate should clearly increase with respect to the off-resonant case. Contrarily, if Rydberg excitation was not accomplished the population of the $4D_{5/2}$ will decay at a low rate to the $5S_{1/2}$ state. In this case the $5S_{1/2} \leftrightarrow 5P_{1/2}$ fluorescence rate will be unaffected by the spectroscopic scan of the Rydberg excitation laser.

Finally, I want to conclude with the saying on the first page, which translates as:

Everyone said "That is not possible."
Then one came, who didn't know, and did it.

In my view this is the best way to describe the current state of quantum physics research. Almost 70 years ago, when the first mechanical computers were built, no-one would have believed that people would be able to trap, manipulate and even perform calculations with single ions. Nowadays, we already deal with the scalability problem of such systems and I think trapped, Rydberg ions present a promising approach to solve this problem.

Appendix A

ABCD-matrix formalism – a Mathematica program

The ABCD-matrix analysis is a geometrical method to calculate how light beams are modified by propagation through optical elements. This technique represents the state of a light beam at a point z through a vector with two parameters: it's distance r to the optical axis and included angle α.

$$\vec{r}(z) = \begin{pmatrix} r(z) \\ \alpha(z) \end{pmatrix}$$

In the paraxial approximation, $sin(\alpha) \approx tan(\alpha) \approx \alpha$, two state vectors at different position values z are linearly connected. This linear relation is described by so called "ray transfer matrices" (or ABCD-matrices), defined by the properties of the corresponding optical element. The input ray vector is multiplied with this matrix to obtain the output vector, which then contains all beam properties modified by the propagation through the element.

$$\begin{pmatrix} r_2 \\ \alpha_2 \end{pmatrix} = \begin{pmatrix} A & B \\ C & D \end{pmatrix} \begin{pmatrix} r_1 \\ \alpha_1 \end{pmatrix}$$

Analogously, the evolution of a Gaussian beam, with initial q-parameter q_1, is described by

$$\begin{pmatrix} q_2 \\ 1 \end{pmatrix} = \begin{pmatrix} A & B \\ C & D \end{pmatrix} \otimes \begin{pmatrix} q_1 \\ 1 \end{pmatrix} \quad \Rightarrow \quad q_2 = \frac{Aq_1 + B}{Cq_1 + D} \tag{A.1}$$

Consecutive propagation through more than one element is described by multiplying the corresponding ABCD-matrices. Since multiplication of matrices is non-commutative the order of the matrices is important: The matrix of the optical element passed first is sited at the first place from the right side so that it acts first onto the input beam. Some important ray transfer matrices:

- Propagation over a distance d in free space or in a medium of constant n: fs(d) $\equiv \begin{pmatrix} 1 & d \\ 0 & 1 \end{pmatrix}$
- Refraction on a planar boundary, with initial refractive index n_1 and final refractive index n_2: plan(n_1, n_2) $\equiv \begin{pmatrix} 1 & 0 \\ 0 & \frac{n_1}{n_2} \end{pmatrix}$
- Propagation through a thin lens: lens(f) $\equiv \begin{pmatrix} 1 & 0 \\ -\frac{1}{f} & 1 \end{pmatrix}$

The target beam parameters for our setup were calculated with the following Mathematica program. The computation of q-parameters and corresponding waists is demonstrated on the example of the 1000 nm beam.

– – – – Mathematica file TOP – – – –

Basic functions to characterize the beam

(* q-paramter at distance z from the minimum beam waist, with Rayleigh length z_0. $R(z)$ is the radius of curvature, $w(z)$ the beam size (radius) at position z, and λ the wavelength *)

q(z) = z + iz_0

$\frac{1}{q(z)} = \frac{1}{R(z)} - i\,\frac{\lambda}{\pi w(z)^2}$

(* definition of q via R and w *)

qd[R_, w_, λ_]:= $\left(\frac{1}{R} - \frac{i\lambda}{\pi w^2}\right)^{-1}$;

(* distance from minimum beam waist *)

z[q_]:=N[Re[q]];

(* Rayleigh length *)

z_0[q_]:=N[Im[q]];

(* Radius of curvature at this position *)

R[q_]:=N[1/Re[1/q]];

(* beam size at this position *)

w[q_, λ_]:=$N\left[\sqrt{\left(\frac{-\lambda}{\pi \mathrm{Im}\left[\frac{1}{q}\right]}\right)}\right]$;

(* minimum beam waist *)

w_0[q_, λ_]:=$w[q - z[q], \lambda]$;

(* divergence angle *)

θ[q_, λ_]:=$N\left[\frac{\lambda}{\pi w_0[q,\lambda]}\right]$;

ABCD matrix formalism (see e.g. Saleh, Teich, page 28/29 & 99)

(* calculating the output q-parameter via the transfer matrix T. T[[1,1]] denotes the matrix entry of the 1st line, 1st row (c.f Eq. (A.1)). *)

ABCD[T_, q_]:=Module[{}, $\frac{T[[1,1]]q+T[[1,2]]}{T[[2,1]]q+T[[2,2]]}$]

(* ABCD of propagation through d m of free space or medium with constant refractive index *)

fs[d_]:= $\begin{pmatrix} 1 & d \\ 0 & 1 \end{pmatrix}$;

(* refraction on planar boundary with initial refractive index n1 and final refractive index n2 *)

plan[n2_, n1_]:= $\begin{pmatrix} 1 & 0 \\ 0 & \frac{n1}{n2} \end{pmatrix}$;

Definitions

(* wavelength of propagating beam in m *)

$\lambda = 1000\ 10^{-9}$;

(* target waist in the center of the crystal, so that zR =7.042253521 mm *)

wC = Sqrt[$\lambda * 7.042253521 * 10\text{^}(-3)/\pi$];

(* half the crystal length in m *)

d2 = 0.02;

(* refractive index of the crystal: 2.21 for 1551 nm, 2.23 for 1000 nm)

nC = 2.23;

Calculation of optimum parameters

(* q-parameter of the beam at the crystal center when zR=7.042253521mm *)

qC = N[qd[∞, wC, λ]]

$0.0 + 0.00704225i$

(* waist inside the crystal, when z_R=7.042253521mm *)

wC

0.0000473457

(* q-parameter of the beam at the outer border of the crystal when z_R=7.042253521mm *)

q2 = ABCD[plan[1, nC].fs[d2], qC]

$0.00896861 + 0.00315796i$

(* waist in free space, when z_R=7.042253521mm *)

$\mathrm{w7} = w_0[\mathrm{q2}, \lambda]$

0.0000317051

Measurements

(* Measured q-parameter of 1000nm in free space at the second lens *)

$\mathrm{q3} = -0.214441 + 0.00278552i$

(* corresponding beam waist of 1000nm in free space *)

$\mathrm{w3} = w_0[\mathrm{q3}, \lambda]$

0.0000297768

(* q-parameter of 1000 nm at the outer crystal border (q3 propagating 0.205 m through free space). Considering measurement errors, this coincides with the target value q2. *)

$\mathrm{q4} = \mathrm{ABCD}[\mathrm{fs}[0.205], \mathrm{q3}]$

$-0.009441 + 0.00278552i$

(* q-parameter of 1000 nm at the crystal center: q4 refracted at the planar crystal border and propagates over 0.02 m to the crystal center *)

$\mathrm{q5} = \mathrm{ABCD}[\mathrm{fs}[0.02].\mathrm{plan}[\mathrm{nC}, 1], \mathrm{q4}]$

$-0.00105343 + 0.00621171i$ (* the beam focus lies 1 mm before the crystal center *)

(* focusing strength of 1000 nm inside the crystal *)

$\mathrm{xi} = 0.04/(2 * \mathrm{Im}[\mathrm{q5}])$

3.21973 (* close to the target value of 2.84 *)

– – – – mathematica file BOTTOM – – – –

From q5, one notices that the measured beam focus lies 1 mm before the center of the crystal. Since this lies within our distance measurement error, it is ignored. Within the measurement errors, the determined q-parameter q4 at the outer border of the crystal matches with the target parameter q2. The same is valid for the focusing parameter xi.

Appendix B

Matching q-parameters – a Mathematica program

The following code is adapted from Stephanie Grabher (group of G. Weihs) and is used to find appropriate telescope parameters (focal lengths f and distances d) for shaping a beam to an arbitrary q-parameter. The plot at the end of the file contains the five telescope parameters (d1,d2,d3,f1,f2), adjustable by the shifting bars and arrow buttons. The functions in the graph denote the theoretically optimal q-parameter (blue) and the initial q-parameter of the beam to match (red). The first kink in the red curve results from the first lens, which enlarges the beam size. The second kink denotes the effect of the second lens, which focuses the beam down. The focusing lengths and lens distances are adapted until the two curves overlap.

– – – – Mathematica file TOP – – – –

Mode matching beam q0 with q-parameter qM

(* initial q-parameter of the 1000 nm beam at the collimator output *)

$\text{q0} = 0.35064 + 0.33069i;$

(* target q-parameter at the crystal surface *)

$\text{qM} = 0.00896861 + 0.00315796i;$

(* wavelength of the beam to match *)

$\lambda = 1000 * 10\text{^}(-9);$

(* Rayleigh lengths and beam waists of the corresponding q-parameters *)

$\text{zR0} = \text{Im}[\text{q0}];$

$\text{zRM} = \text{Im}[\text{qM}];$

$\text{wo0} = \text{Sqrt}[\lambda * \text{zR0}/\pi] * 10\text{^}6;$

$\text{woM} = \text{Sqrt}[\lambda * \text{zRM}/\pi] * 10\text{^}6;$

(* beam size at the distance z from the beam waist *)

w[z_, q_]:=Sqrt[λ * Im[q]/π] * Sqrt[1 + (z/Im[q])^2];

(* d1: distance between collimator and first lens, d2: spacing between the two lenses, d3: distance between lens and crystal surface, f1 and f2: focal lengths of first and second lens *)

Manipulate[

q1 = q0 + d1

q2 = q1/(−q1/f1 + 1);

q3 = q2 + d2;

q4 = q3/(−q3/f2 + 1);

q5 = q4 + d3;

$$\text{Plot}[\{10\text{^}6 * \text{Evaluate}\left[\left\{\begin{array}{ll} w[z + \text{Re[q0]}, \text{q0}] & z < \text{d1} \\ w[z - \text{d1} + \text{Re[q2]}, \text{q2}] & \text{d1} < z < \text{d1} + \text{d2} \\ w[z - \text{d1} - \text{d2} + \text{Re[q4]}, \text{q4}] & \text{d1} + \text{d2} < z < \text{d1} + \text{d2} + \text{d3} + 0.05 \end{array}\right.\right],$$

$10\text{^}6 * w[-z + \text{d1} + \text{d2} + \text{d3} + \text{Re[qM]}, \text{qM}]\}, \{z, 0, \text{d1} + \text{d2} + \text{d3} + 0.05\},$

PlotStyle → {{Red, Thick}, {Blue, Thick}}] ,

(* selectable values for d and f *)

{d1, 0.01, 0.7}, {d2, 0.01, 0.7}, {d3, 0.01, 0.7}, {f1, {0.010, 0.012, 0.015, 0.020, 0.025, 0.0254, 0.030, 0.035, 0.040, −0.050, 0.060, 0.075, 0.085, 0.090, 0.100, 0.125, 0.150, 0.175, 0.200, 0.250, 0.300, 0.400, 0.500, 0.750, 0.1000}}, {f2, {0.010, 0.012, 0.015, 0.020, 0.025, 0.0254, 0.030, 0.035, 0.040, 0.050, 0.060, 0.075, 0.085, 0.090, 0.100, 0.125, 0.150, 0.175, 0.200, 0.250, 0.300, 0.400, 0.500, 0.750, 0.1000}}]

(* Diagram window with adjustable parameters, to match the q-parameters graphically. Here, the beam waist is plotted (in micrometres) as a function of the distance to the collimator (in metres). The blue function denotes the theoretically optimal q-parameter, whereas the red line is the current q-parameter of the actual beam to match. For the example of the 1000 nm beam, the optimum telescope parameters are: f1=-50 mm, f2=100 mm, distance between collimator and first lens d1=9.7 cm, lens spacing d2=13.9 cm and distance between second lens and crystal surface d3=20.5 cm. *)

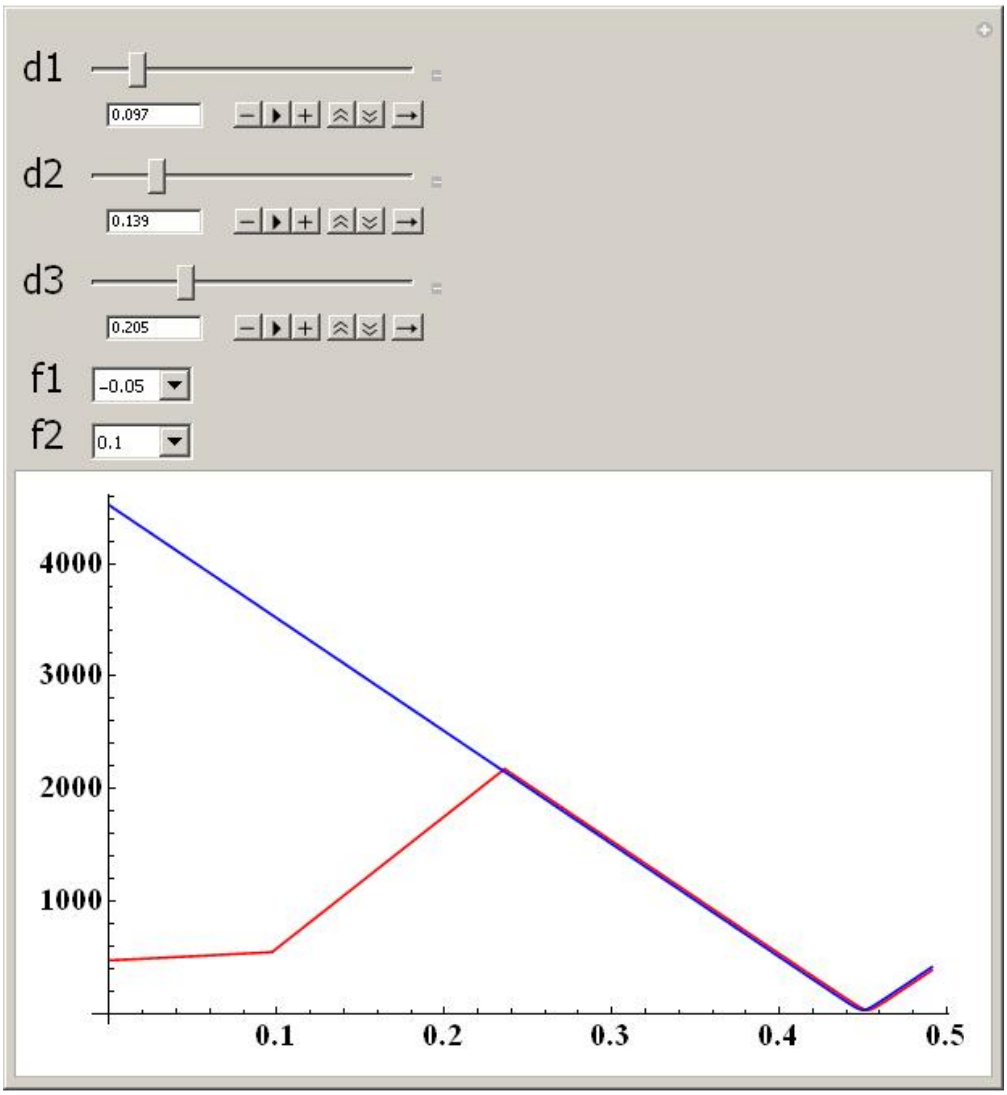

– – – – Mathematica file BOTTOM – – – –

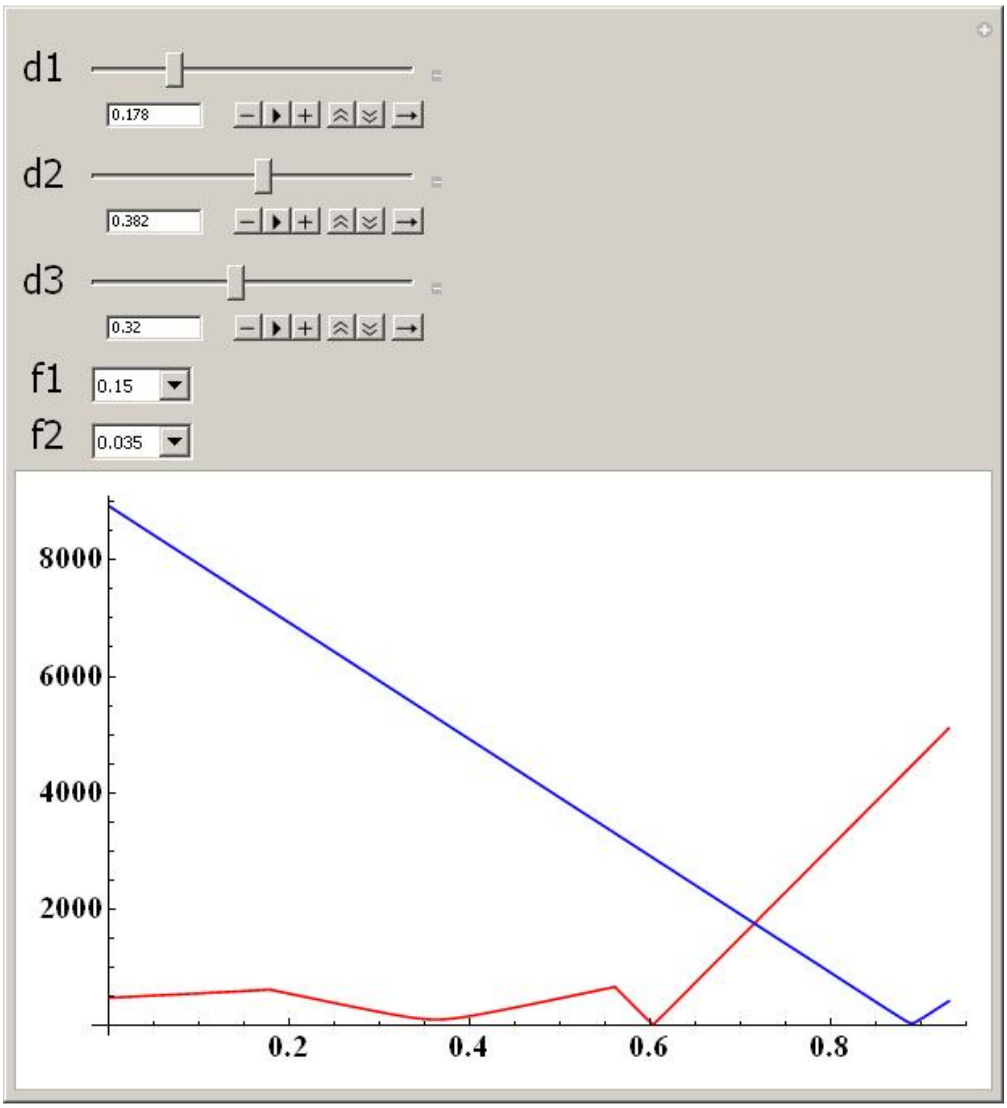

Figure B.1: Diagram window with adjustable parameters as an example for non-matched q-parameters. Blue: theoretically optimal q-parameter, Red: initial q-parameter of the beam to match.

Bibliography

[1] D. P. Di Vincenzo, *Mesoscopic Electron Transport*, NATO Advanced Study Institute, Series E: Applied Sciences, edited by L. Sohn, L. Kouwenhoven, and G. Schoen, **345** (1996), URL http://arxiv.org/abs/cond-mat/9612126.

[2] H. C. Nägerl, D. Leibfried, H. Rohde, G. Thalhammer, J. Eschner, F. Schmidt-Kaler, and R. Blatt, Phys. Rev. A **60**, 145 (1999), URL http://link.aps.org/doi/10.1103/PhysRevA.60.145.

[3] R. Blatt and D. Wineland, Nature **453**, 1008 (2008), URL http://www.nature.com/nature/journal/v453/n7198/full/nature07125.html.

[4] J. Benhelm, G. Kirchmair, C. F. Roos, and R. Blatt, Nature Physics **4**, 463 (2008), URL http://www.nature.com/nphys/journal/v4/n6/full/nphys961.html.

[5] H. Häffner, C. F. Roos, and R. Blatt, Phys. Rep. **469**, 155 (2008), URL http://www.sciencedirect.com/science/article/pii/S0370157308003463.

[6] T. Monz, P. Schindler, J. T. Barreiro, M. Chwalla, D. Nigg, W. A. Coish, M. Harlander, W. Hänsel, M. Hennrich, and R. Blatt, Phys. Rev. Lett. **106**, 130506 (2011), URL http://link.aps.org/doi/10.1103/PhysRevLett.106.130506.

[7] T. F. Gallagher, Rep. Prog. Phys. **51**, 143 (1988), URL http://iopscience.iop.org/0034-4885/51/2/001.

[8] M. Müller, L.-M. Liang, and P. Lesanovsky, I. Zoller, New J. Phys. **10**, 093009 (2008), URL http://arxiv.org/abs/0709.2849.

[9] D. Leibfried, R. Blatt, C. Monroe, and D. Wineland, Rev. Mod. Phys. **75**, 281 (2003), URL http://rmp.aps.org/abstract/RMP/v75/i1/p281_1.

[10] D. Jaksch, J. I. Cirac, P. Zoller, S. L. Rolston, R. Côté, and M. D. Lukin, Phys. Rev. Lett. **85**, 2208 (2000), URL http://link.aps.org/doi/10.1103/PhysRevLett.85.2208.

[11] M. A. Nielsen and I. L. Chuang, *Quantum Computation and Quantum Information* (Cambridge University Press, Cambridge, England, 2000), ISBN 978-1-107-00217-3.

[12] L. Isenhower, E. Urban, X. L. Zhang, A. T. Gill, T. Henage, T. A. Johnson, T. G. Walker, and M. Saffman, Phys. Rev. Lett. **104**, 010503 (2010), URL http://link.aps.org/doi/10.1103/PhysRevLett.104.010503.

[13] B. T. Torosov and N. V. Vitanov, J. Phys. B **45**, 135502 (2012), URL http://iopscience.iop.org/0953-4075/45/13/135502.

[14] F. Schmidt-Kaler, T. Feldker, D. Kolbe, J. Walz, M. Müller, P. Zoller, W. Li, and L. I., New J. Phy. **13**, 1367 (2011), URL http://iopscience.iop.org/1367-2630/13/7/075014.

[15] C. G. Parthey, A. Matveev, J. Alnis, B. Bernhardt, A. Beyer, R. Holzwarth, A. Maistrou, R. Pohl, K. Predehl, T. Udem, et al., Phys. Rev. Lett. **107**, 203001 (2011), URL http://link.aps.org/doi/10.1103/PhysRevLett.107.203001.

[16] A. C. Wilson, C. Ospelkaus, A. P. VanDevender, J. A. Mlynek, K. R. Brown, D. Leibfried, and D. J. Wineland, Appl. Phys. B **105**, 741 (2011), URL http://arxiv.org/abs/1105.5356.

[17] V. Lange, M. A. Khan, U. Eichmann, and S. W., Z. Phys. D - Atoms, Molecules and Clusters **18**, 319 (1991), URL http://link.springer.com/article/10.1007%2FBF01426593.

[18] M. Aymar, C. H. Greence, and E. Luc-Koenig, Rev. Mod. Phys. **68**, 1015 (1996), URL http://link.aps.org/doi/10.1103/RevModPhys.68.1015.

[19] H. S. Friedrich, *Theoretical Atomic Physics 3rd ed* (Berlin: Springer, 2005), ISBN 3-540-54179-9.

[20] U. I. Safronova, Phys. Rev. A **82**, 022504 (2010), URL http://link.aps.org/doi/10.1103/PhysRevA.82.022504.

[21] J. Branson, *Quantum Mechanics, Physics 130A*, University of California, San Diego (November 2013), URL http://quantummechanics.ucsd.edu/ph130a/130_notes/node424.html.

[22] R. W. Boyd, *Nonlinear Optics* (Academic Press, 1992), ISBN 0121216802.

[23] F. Zernike and J. E. Midwinter, *Applied Nonlinear Optics* (Wiley Interscience, 1973), ISBN 0471982121.

[24] H. H. Niedrig, *Bergmann/Schaefer: Lehrbuch der Experimentalphysik Band 3. Optik* (de Gruyter, 1993), ISBN 3110129736.

[25] J. A. Giordmaine, Phys. Rev. Lett. **8**, 19 (1962).

[26] P. D. Maker, R. W. Terhune, M. Nisenoff, and C. M. Savage, Phys. Rev. Lett. **8**, 21 (1962), URL http://link.aps.org/doi/10.1103/PhysRevLett.8.21.

[27] F. J. Zernike, JOSA **54**, 1215 (1964), URL http://www.opticsinfobase.org/josa/abstract.cfm?id=52481.

[28] M. Polyanskiy, *RefractiveIndex.INFO* (August 2013), URL http://refractiveindex.info/?group=CRYSTALS&material=KH2PO4.

[29] R. U. Nijmegen, *Optical Parametric Oscillator* (August 2013), URL http://www.ru.nl/tracegasfacility/trace_gas_research/laser-sources/optical-parametric/.

[30] A. Ferguson, *Nonlinear Optics - Quasi-phase-matching* (August 2013), URL http://phys.strath.ac.uk/12-370/sld047.htm.

[31] A. Gayer, Z. Sacks, E. Galun, and A. Arie, Appl. Phys. B **91**, 343 (2008), URL http://link.springer.com/article/10.1007%2Fs00340-008-2998-2.

[32] D. H. Jundt, Opt. Lett. **22**, 1553 (1997), URL http://dx.doi.org/10.1364/OL.22.001553.

[33] U. Schlarb and K. Betzler, Phys. Rev. B **48**, 15613 (1993), URL http://link.aps.org/doi/10.1103/PhysRevB.48.15613.

[34] L. E. Myers, R. C. Eckardt, M. M. Fejer, R. L. Byer, W. R. Bosenberg, and J. W. Pierce, JOSAB **12**, 2102 (1995), URL http://dx.doi.org/10.1364/JOSAB.12.002102.

[35] G. D. Boyd and D. A. Kleinman, J. Appl. Phys. **39**, 3597 (1968), URL http://dx.doi.org/10.1063/1.1656831.

[36] J. R. M.-L. Schwesyg, *Interaction of light with impurities in lithium niobate crystals*, Rheinischen Friedrich-Wilhelms-Universität Bonn, Ph.D. thesis (2011).

[37] TOPTICA Photonics AG, *TA/DL-SHG pro, Frequency Doubled High Power Laser System, Manual* (2009).

[38] R. W. P. Drever, J. L. Hall, F. V. Kowalski, J. Hough, G. M. Ford, A. J. Munley, and H. Ward, Appl. Phys. B **31**, 97 (1983), URL http://link.springer.com/article/10.1007/BF00702605.

[39] E. D. Black, Am. J. Phys. **69**, 79 (2001), URL http://dx.doi.org/10.1119/1.1286663.

Acknowledgements

I want to take this opportunity to thank everyone who has contributed to the realization of this work. Every single one of you played an essential role and was a great help; technically or psychologically.
I thank Markus Hennrich for giving me the opportunity to take part in setting up a totally new experiment, it was a great experience and adventure. Your patience and pleasure while explaining physical phenomena, especially complex ones, was tremendously inspiring and motivating. I also want to thank you for all the effort you have put into reading and correcting this thesis even under pressure of time.
Special gratitudes go to the young physicists Gerard Higgins and Fabian Pokorny, for our great time together in the lab. Not only were you unconditionally helpful concerning theoretical and experimental troubles but you also created a comfortable atmosphere, loosing stressful days with funny discussions about non-scientific subjects and a cup of tea. It was a pleasure to set up the lab with you and I am looking forward to hear ground-breaking results! Moreover, thank you Gerard for your advice concerning the English language and for continuing the stabilization work on the "Halfling", even on weekends.
Many thanks also to the other members of Rainer Blatt's group, especially the cooking group, the Rocket Society and the office-crew Fabian, Kirsten and Philip, for all the interesting discussions from which I learned a lot about physics, science, and surprisingly history too.

I would also like to thank Christian. Since the first "Proseminar" sheet you always supported me in the studies but especially in everyday life. Your encouragement and motivation in difficult moments was irreplaceable and so are our many happy moments. I am deeply thankful that we have found each other and I am looking forward to our common future.
Finally, I thank my brother and my sisters, and especially my parents, for providing me all the opportunities I have had in life and for supporting all my decisions. It was not your financial rather but your psychological support and encouragement which allowed me to become what I am today. You raised me to a happy, self-confident, strongly motivated person!

Eidesstattliche Erklärung

Ich erkläre hiermit an Eides statt durch meine eigenhändige Unterschrift, dass ich die vorliegende Arbeit selbständig verfasst und keine anderen als die angegebenen Quellen und Hilfsmittel verwendet habe. Alle Stellen, die wörtlich oder inhaltlich den angegebenen Quellen entnommen wurden, sind als solche kenntlich gemacht.

Die vorliegende Arbeit wurde bisher in gleicher oder ähnlicher Form noch nicht als Magister-/Master-/Diplomarbeit/Dissertation eingereicht.

Datum	Unterschrift